Chapter 3

Chapter 3

Mechanistic Insight into the Inhibition of Choline Acetyltransferase by Proton Pump Inhibitors

3.1. Introduction

PPIs are among the top ten prescribed medications in the world and are broadly prescribed for the management of various gastrointestinal disorders like ulcers, gastroesophageal reflux disease, and Helicobacter pylori infection (1). Omeprazole was the first PPI to be clinically approved and used followed by the approval of Lansoprazole, Pantoprazole, Rabeprazole, Ilaprazole, and Tenatoprazole (2) (**Figure 3.1**). They are structurally similar and contain a benzimidazole and a pyridine ring with different substitutions and thus exhibit similar pharmacological properties (3). There have been several reports showing that PPIs are able to cross the blood−brain barrier (BBB) and thereby reach the CNS in experimental animals (3, 4).

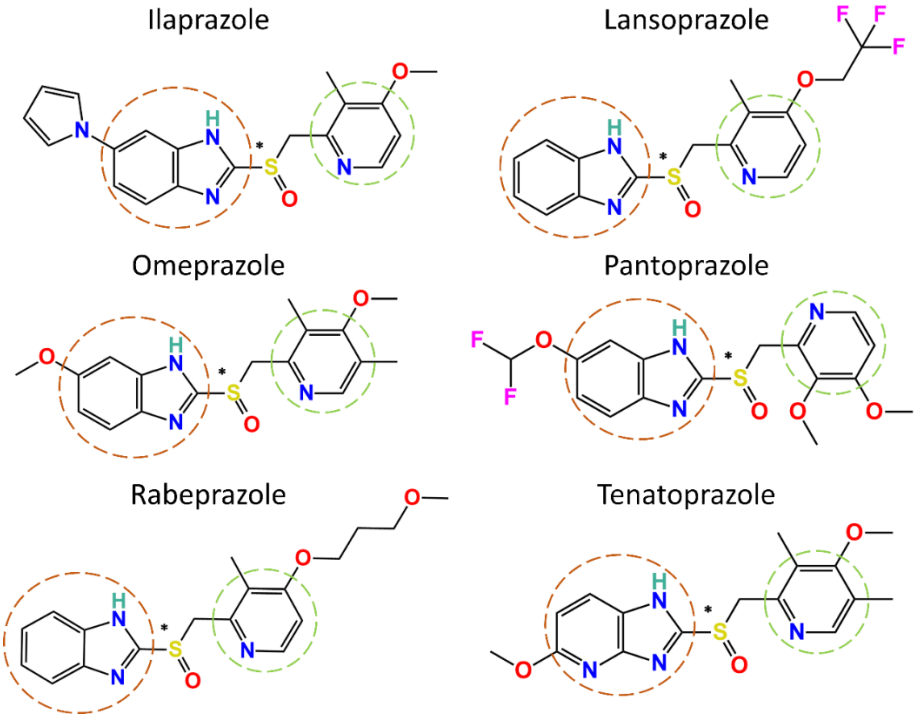

Figure 3.1. PPIs Benzimidazole moiety is shown in brown circle (4-Azabenzimidazole for the Tenatoprazole) and the pyridine ring is shown in green circle. The Sulphur atom marked '*' is

the chiral center of the PPIs and thus exists in a racemic mixture of 2 enantiomers 'R' and 'S'. PPIs have been reported to have negative effects on cognition and their prolonged use is shown to be associated with an increased prevalence of dementia (5, 6). A couple of epidemiological studies, two from Germany (7) and one from Taiwan, (8-10) concluded that long-term exposure to PPIs may increase the incidence of developing dementia especially in the elderly. In a recent study, Lam et al. reported a significant association of PPI use with vitamin B12 deficiency in a population-based sample, which has been known to play a role in cognitive decline. Furthermore, PPIs have also been shown to enhance Aβ levels in animal studies by modulating the β- and γ-secretase enzymes. Aβ peptides interact with and modulate various components within the cholinergic system like AChE, BuChE, the high affinity choline transporter, and the acetylcholine biosynthesizing enzyme ChAT (11). Recently, we reported an unprecedented mode of action of PPIs, where these drugs seem to exhibit potent inhibitory activity on the core cholinergic enzyme ChAT, thus indicating a possible link between PPI use and the increase in risk for dementia due to the reduction in acetylcholine biosynthesis (12).

ChAT is a globular protein, responsible for biosynthesis of acetylcholine. It is an explicit marker of cholinergic cells and might therefore be the most appropriate biomarker for tracking the functional condition of the cholinergic neurons within the central and peripheral nervous systems (13). In the search for useful imaging biomarkers, we have focused on the cholinergic neuronal system due to its involvement in cognitive functions like learning, memory, and sleep, as well as in neuromotor function. There is evidence for specific loss of central cholinergic neurons in the basal forebrain of patients diagnosed with Alzheimer's disease (14). There are only a few ChAT ligands known and still fewer well characterized compounds are available regardless of its discovery a century ago. All the previously reported ligands were found to be inhibitors of the enzyme, including derivatives of naphthylvinylpyridine, stilbazole, (15) alkylaminoethyl esters, and 2-(α-naphthoyl) ethyltrimethylammonium iodide (α-NETA) (16).

However, these ligands exhibit poor pharmacokinetic and pharmacodynamics properties due to the presence of quaternary amines as a permanent charge bearing moiety in their structure, which also hinders their ability to cross the BBB.

We have recently reported that PPIs bind to ChAT with high affinity and by doing so inhibit the enzyme. Therefore, we aim in this study to further gain knowledge about their mode of interaction with the binding pocket. Moreover, as the PPIs showed a mixed-competitive mode of action in our in-vitro studies, we focused on the interaction of the PPIs with amino acid residues, particularly HIS324, which is the catalytic residue in the substrate binding pocket of the ChAT enzyme (17).

Therefore, the main objective of the present study is to gain mechanistic insight into the precise molecular interactions of PPIs with ChAT and to explore their impact as potential PET ligands with the help of molecular docking and classical molecular dynamics simulations. Such insight is crucial for developing new compounds with high affinity, high selectivity, and optimal physicochemical properties that can be used as molecular probes of the ChAT distribution in the brain for diagnosis of cholinergic neurodegenerative diseases such as AD and different neuromotor disorders, in particular ALS, at their early stages.

3.2. Objectives

The objectives of this study are as follows:

- **In silico molecular docking studies**: To gain mechanistic insight about precise molecular interactions of how PPIs interact within the binding tunnel of ChAT enzyme. Molecular docking against ChAT enzyme were carried out.
- **In silico molecular dynamics studies**: Further to understand the crucial dynamic behavior of the complex formation process of PPIs with ChAT we performed extensive classical molecular dynamics simulation.
- **Residue interaction analysis**: To understand the interaction of PPIs with the catalytic

amino acid residue of ChAT, we extracted the energy minima complex obtained from the MD simulation and performed the Residue interaction network analysis revealing the interaction with HIS324 residue.

- **Molecular Mechanics Poisson−Boltzmann Surface Area Analysis**: To understand the dynamic binding affinity of the PPIs with ChAT we calculated the binding free energy of the formed complexes post MD simulations.
- **In Silico BBB Permeability Analysis**: To check if the PPIs hold the potential to cross blood brain barrier, we analyzed the PPIs for in silico prediction of BBB permeability

3.3. Results and Discussions

3.3.1. Molecular Docking Study

For validating the docking methodology, we have re-docked the choline ligand that was bound to the ChAT catalytic tunnel in the crystal structure (PDB ID: 2FY3) and the superimposed view is shown in **Figure 3.2** having a GScore value of −3.673 kcal/mol. The root mean square deviation (RMSD) value of the re-docked pose was computed to be about 2.45 Å, which is fairly acceptable for the given scenario as the active binding catalytic tunnel of ChAT is big and the choline molecule is a small ligand, thus indicating that the docking methodology used for the study generates reliable results. The PPIs were docked into the binding pocket of ChAT, which generated three most probable binding poses for each PPI. The docked poses were manually inspected for the interaction that takes place and for the specific docking pose of the PPIs bound to the ChAT. The pyridine ring that is a common structure in all PPI molecules seems to be interacting with the catalytic amino acid residue, HIS324. This might be pointing at the mechanism of inhibition of ChAT by these drugs. The primary docking pose was finally selected based on above-mentioned criteria along with having the best docking score out of the three poses (**Figure 3.3, 3.4 and 3.5**). The GScore of these selected docked poses are shown in

bold in **Table 3.1**.

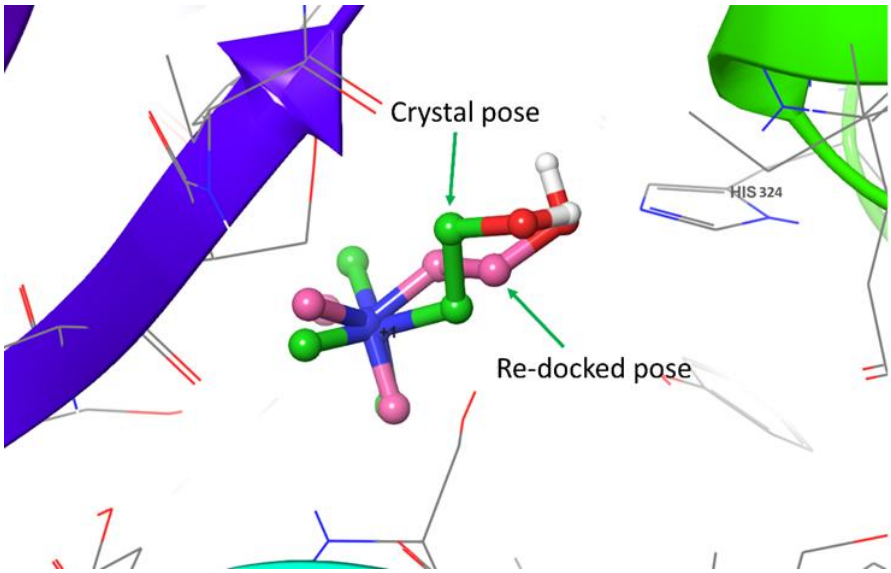

Figure 3.2. 3D re-docking pose of choline in comparison to the crystal structure pose

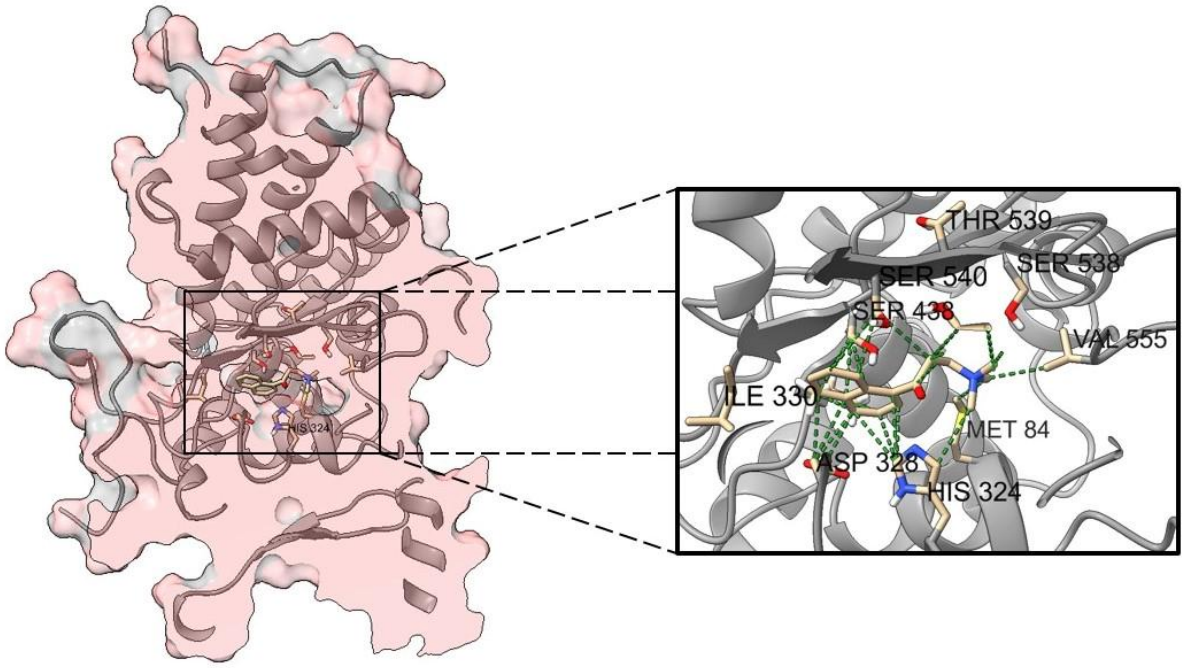

Figure 3.3. 3D-docking poses for α-NETA as the classical ChAT inhibitor, which is used as a reference compound for comparison in the study

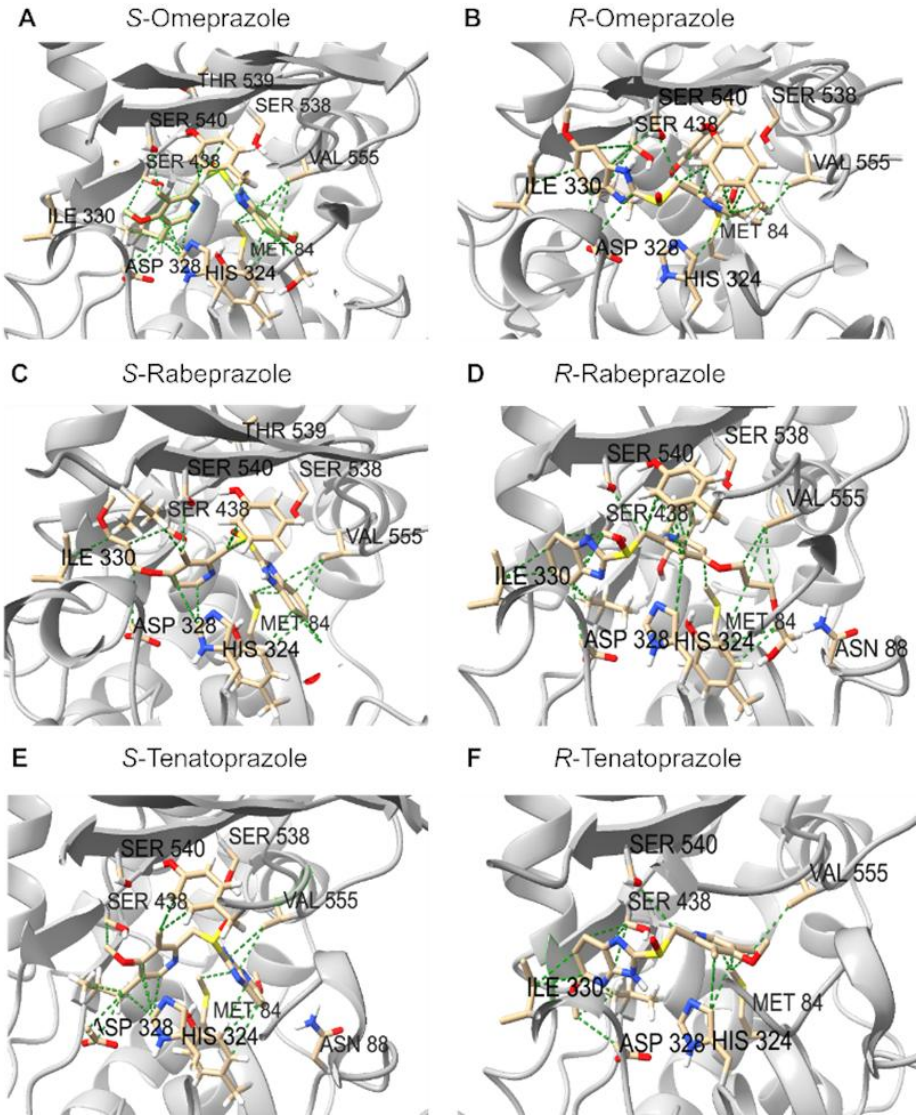

Figure 3.4. Comparison of the selected 3D-docking poses for stereoisomers of Omeprazole, Rabeprazole, and Tenatoprazole with ChAT. (A) Selected 3D poses for the stereoisomer *S*-Omeprazole with ChAT, (B) 3D binding pose for *R*-Omeprazole with ChAT, (C) 3D binding pose for *S*-Rabeprazole with ChAT, (D) 3D binding pose for *R*-Rabeprazole with ChAT, (E) 3D binding pose for *S*-Tenatoprazole with ChAT, (F) 3D binding pose for *R*-Tenatoprazole with ChAT. The green dotted lines show the van der Waals interactions.

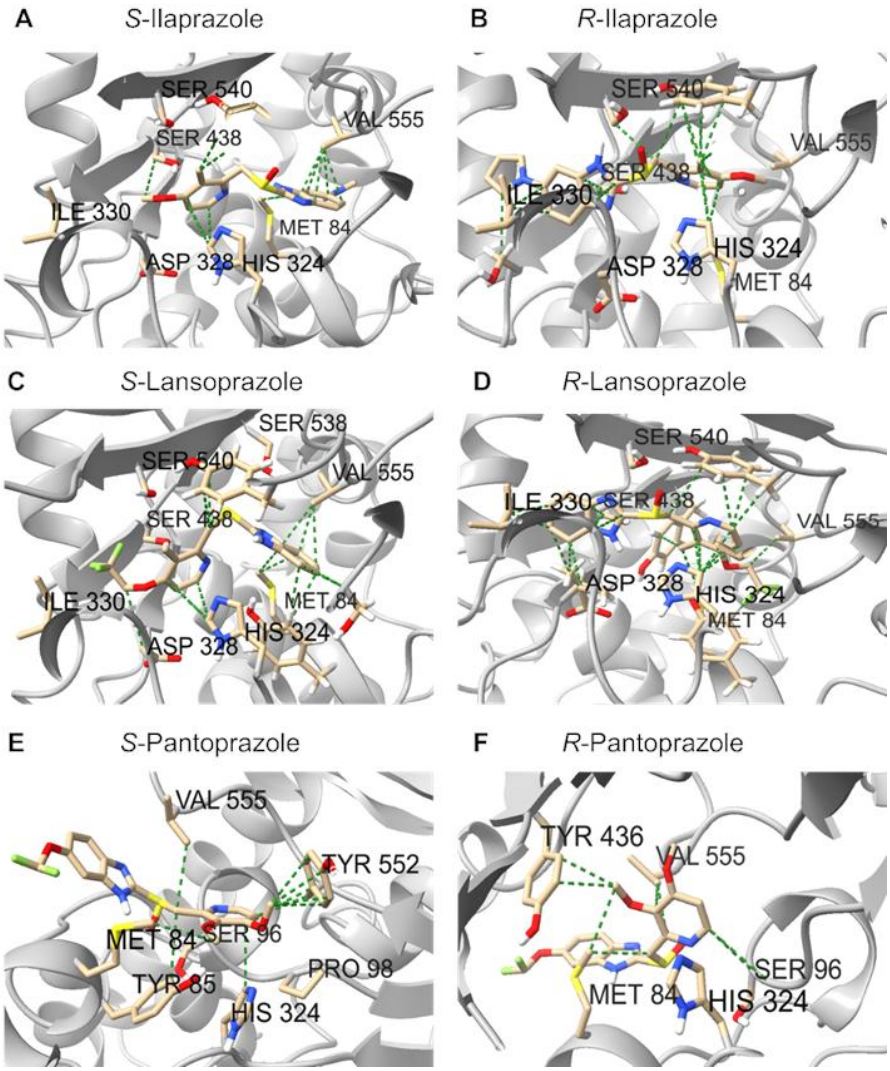

Figure 3.5. 3D docking pose of PPIs with ChAT. A) 3D binding pose for *S*-Ilaprazole with ChAT. B) 3D binding pose for *R*-Ilaprazole with ChAT. C) 3D binding pose for *S*-Lansoprazole. D) 3D binding pose for *R*-Lansoprazole. E) 3D binding pose for *S*-Pantoprazole with ChAT. F) 3D binding pose for *R*-Pantoprazole.

Table 3.1. Molecular docking binding GScore of top three binding pose of PPIs with ChAT protein. More the negative value the stronger is the binding for the PPIs with ChAT. The selected pose based on its interaction is shown in bold.

Sr. No.	Compound	GScore (kcal/mol) Pose1	GScore (kcal/mol) Pose2	GScore (kcal/mol) Pose3
1	α-NETA	**-5.096**	-4.574	-4.462

2	*S*-Ilaprazole	-5.930	-3.999	**-3.987**
3	*R*-Ilaprazole	-5.908	**-2.428**	NA
4	*S*-Lansoprazole	**-6.363**	-6.083	-5.756
5	*R*-Lansoprazole	-7.581	-6.255	**-4.431**
6	*S*-Omeprazole	-5.905	-5.111	**-4.462**
7	*R*-Omeprazole	**-4.428**	-4.244	-1.624
8	*S*-Pantoprazole	-5.197	**-5.108**	-4.525
9	*R*-Pantoprazole	**-6.130**	-5.988	-5.851
10	*S*-Rabeprazole	**-6.007**	-5.843	-5.813
11	*R*-Rabeprazole	**-5.629**	-4.096	-1.445
12	*S*-Tenatoprazole	**-4.037**	-1.364	-1.289
13	*R*-Tenatoprazole	**-6.348**	-5.581	-5.161

For comparisons, we used α-NETA, one of the best-known inhibitors of ChAT that is commercially available. This inhibitor gave a docking score of −5.096 in pose 1, where the ethyltrimethylammonium moiety of α-NETA seems to be in the close vicinity of the HIS324 residue displaying a hydrophobic interaction with it (**Figure 3.3**). Likewise, the GScores for the selected docked poses of PPIs were in the range of −1.289 to −6.363 kcal/mol. Among these, the *S*-lansoprazole, *R*-Pantoprazole, *S*-Rabeprazole, *R*-Rabeprazole, and *R*-Tenatoprazole displayed significantly higher docking scores (−6.363, −6.130, −6.007, −5.629, and −6.348 kcal/ mol, respectively) than α-NETA. The pyridine ring of the S enantiomer of the PPIs was surrounded by ILE330, HIS324, ASP328, SER438, SER540, and THR539, amino acid residues that reside in the geometrical orientation of the PPIs in the ChAT catalytic pocket except for the pyridine ring of S-Pantoprazole which was surrounded by MET84, TYR85, SER96, PRO98, HIS324, and TYR552 amino acid residues. This is likely due to the strong interaction of the methoxy (−OCH3) group substitution present at the fourth position of the pyridine ring of the Spantoprazole with the TYR552 amino acid residue. Likewise, the pyridine ring of the R enantiomer of the PPIs was observed to be surrounded by MET84, HIS324, SER540, SER538,

and VAL555 amino acid residues, thus exhibiting some minor differences between the two R and S conformers of the PPIs. These observations thereby seem to support the notion that the pyridine ring of the PPIs might be crucial for their interaction with the ChAT protein given that a similar phenomenon is also apparent for the classical ChAT inhibitor, α-NETA, through a polar interaction with the HIS324 residue of ChAT. Furthermore, there are some notable differences in the interaction of the benzimidazole moiety of the PPIs with the ChAT where the S enantiomer of the PPIs seems to be surrounded with MET84, SER538, and VAL555 amino acid residues where VAL555 seems to play a major role in the stabilization of the benzimidazole moiety of the S enantiomer of the PPIs in the ChAT catalytic site and thus help in the orientation of the pyridine ring with the HIS324 residue. The benzimidazole ring of the R enantiomer of the PPIs was observed to be enveloped by ILE330, ASP328, and SER438 amino acid residues that seem to stabilize the benzimidazole moiety of the R enantiomer of the PPIs, thus aiding in the orientation of the pyridine ring in line with the HIS324 amino acid residue.

3.3.2. Molecular Dynamics Study

The binding mode predictions for PPIs with ChAT made by the docking analysis were further scrutinized by means of molecular dynamics simulations to gain more insight into the crucial interactions, the three-dimensional conformational changes, and the stability during the simulation time span. The trajectories obtained from a 200 ns long simulation were analyzed for various parameters, and we monitored the RMSD of the simulated system in order to ascertain that 200 ns is a sufficient period of time for the system to become stabilized, signifying that the system reached convergence with no major fluctuation. The RMSD can also be utilized as a measure of the difference of the backbone of the protein from its initial starting position to the final conformation obtained after the simulation. According to literature, an RMSD value

less than 0.25 nm can be regarded to be very close to the reference structure. (18) The RMSD plot of the simulated systems suggests that the ChAT protein remained stable during the 200 ns long simulation (**Figure 3.6**). The RMSD values for the ChAT protein during its complex formation with the compounds seem to be stabilized within a fluctuation range of 0.1 to 0.3 nm, except for the ChAT with tenatoprazole, which was stabilized within 0.4 to 0.5 nm (**Figure 3.6 D**). Nonetheless, these observations indicated that the protein RMSD values were well in the limit with low uncertainties. The RMSD values for the standard compound, α-NETA, and for the PPIs were in the range of 0.1−0.7 nm. This is expected given that small molecules tend to be more flexible in nature, and hence, during their initial interaction with the protein for the complex formation, are constantly subjected to the dynamic changes to achieve the most suitable fit conformation, i.e., to occupy their optimal binding pose at the ChAT protein.

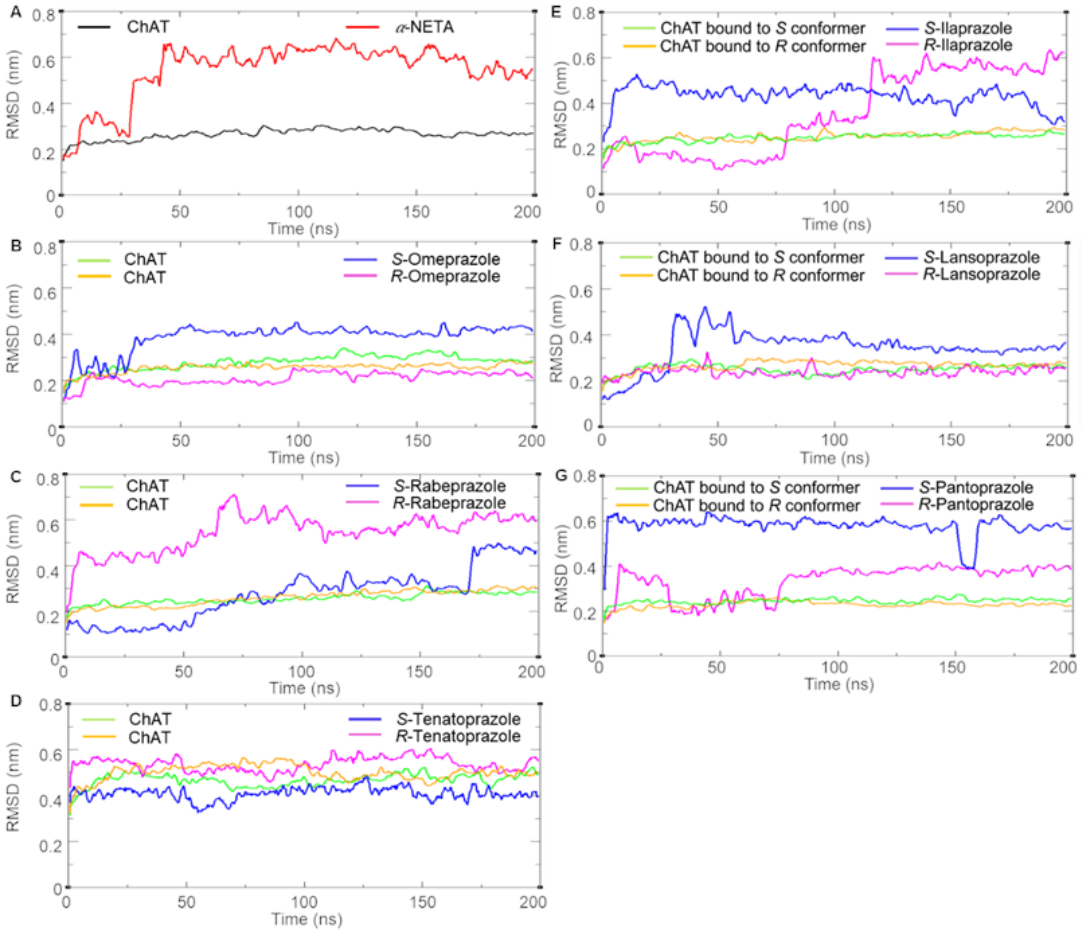

Figure 3.6. RMSD analysis of the 200 ns trajectory obtained from molecular dynamics

simulations. A) Represents the RMSD plot as the function of simulation time frame for the standard α-NETA (red) and ChAT (black) in the complex, B) Shows the RMSD for the *S*-Omeprazole (blue) and *R*-Omeprazole (pink) complexed with ChAT (green and orange respectively), C) Shows the RMSD for the *S*-Rabeprazole (blue) and *R*-Rabeprazole (pink) complexed with ChAT (green and orange, respectively), D) Shows the RMSD for the *S*-Tenatoprazole (blue) and *R*-Tenatoprazole (pink) complexed with ChAT (green and orange respectively). E) Shows the RMSD for the *S*-Ilaprazole (blue) and *R*-Ilaprazole (pink) complexed with ChAT (green and orange respectively). F) Shows the RMSD for the *S*-Lansoprazole (blue) and *R*-Lansoprazole (pink) complexed with ChAT (green and orange respectively). G) Shows the RMSD for the *S*-Pantoprazole (blue) and *R*-Pantoprazole (pink) complexed with ChAT (green and orange respectively).

Next, we analyzed the trajectory for root-mean-square fluctuations (RMSFs) as a function of fluctuation of individual amino acid residues throughout the simulation. Such analysis can identify amino acid residues with a key role in the interaction by assessing their dynamic behavior and their level of flexibility in the ChAT protein structure throughout the simulation time span. The height of the peak indicates the magnitude of residue flexibility and the regions of the protein structure responsible for the major three-dimensional conformational changes that occur during the simulation. The RMSF plots for the ChAT protein were in the range of 0.05 to 0.6 nm, which indicates no major fluctuations in the core structure of the protein (**Figure 3.7**). The C- and N-termini of the ChAT protein show higher RMSF values, up to 1.25 nm, which is expected since they are naturally exposed to the solvent surface and therefore become structurally more flexible.

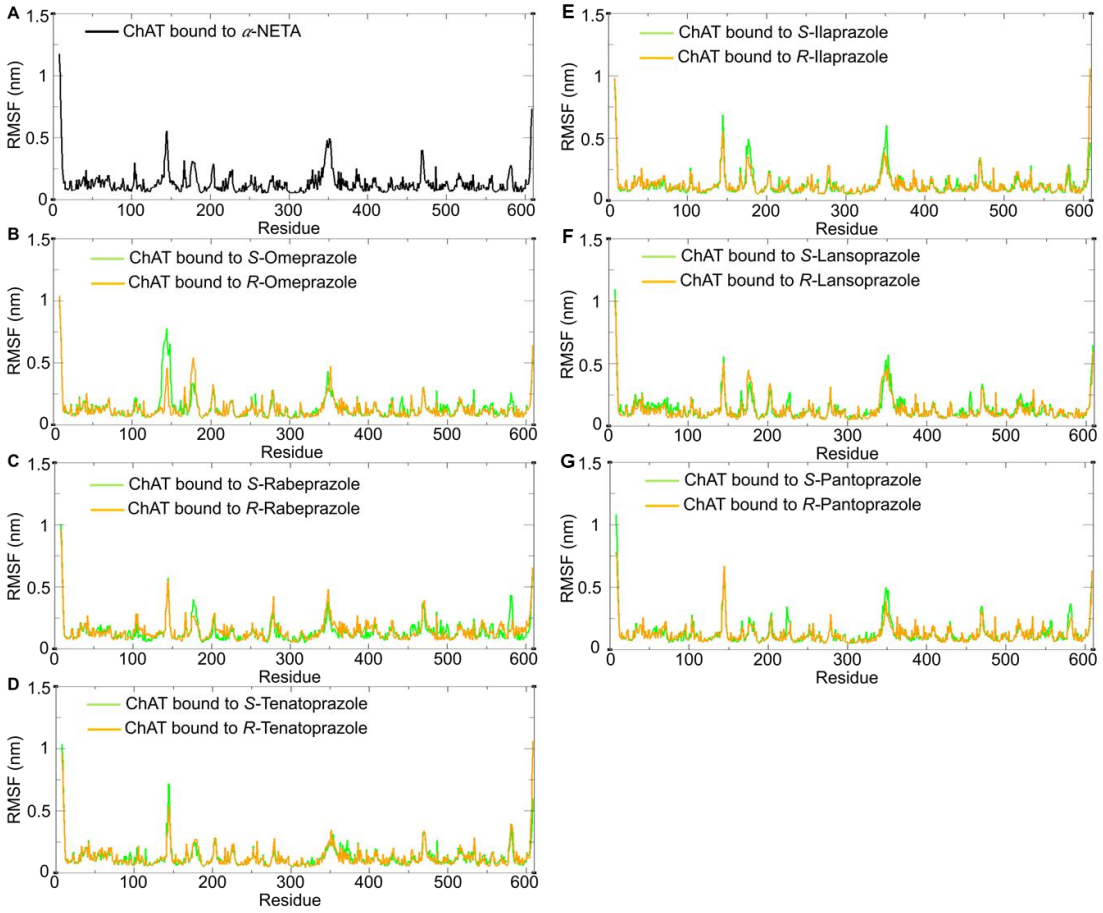

Figure 3.7. RMSF analysis of ChAT protein as a function of individual amino acid of the 200 ns trajectory obtained from molecular dynamics simulation. A) Represents the RMSF plot of ChAT (black) bound to *α*-NETA, B) Shows the RMSF plot of ChAT bound to *S*-Omeprazole (green) and to *R*-Omeprazole (orange), C) Shows the RMSF plot of ChAT bound to *S*-Rabeprazole (green) and to *R*-Rabeprazole (orange), D) Shows the RMSF plot of ChAT bound to *S*-Tenatoprazole (green) and to *R*-Tenatoprazole (orange). E) Shows the RMSF plot of ChAT (green) bound to *S*-Ilaprazole and ChAT (orange) bound to *R*-Ilaprazole. F) Shows the RMSF plot of ChAT (green) bound to *S*-Lansoprazole and ChAT (orange) bound to *R*-Lansoprazole. G) Shows the RMSF plot of ChAT (green) bound to *S*-Pantoprazole and ChAT (orange) bound to *R*-Pantoprazole.

Similarly, the RMSF values for the PPIs were found in the range of 0.01 to 0.3 nm (**Figure 3.8**) indicating a necessary balance between the dynamical stability and flexibility for

accommodating the ligand into binding pocket of the protein during complex formation. The RMSF fluctuation for PPIs (0.01−0.3 nm) was narrower than the corresponding fluctuation for α-NETA (0.05−0.6 nm), which might indicate that the PPIs were bound more firmly to the ChAT protein than α-NETA.

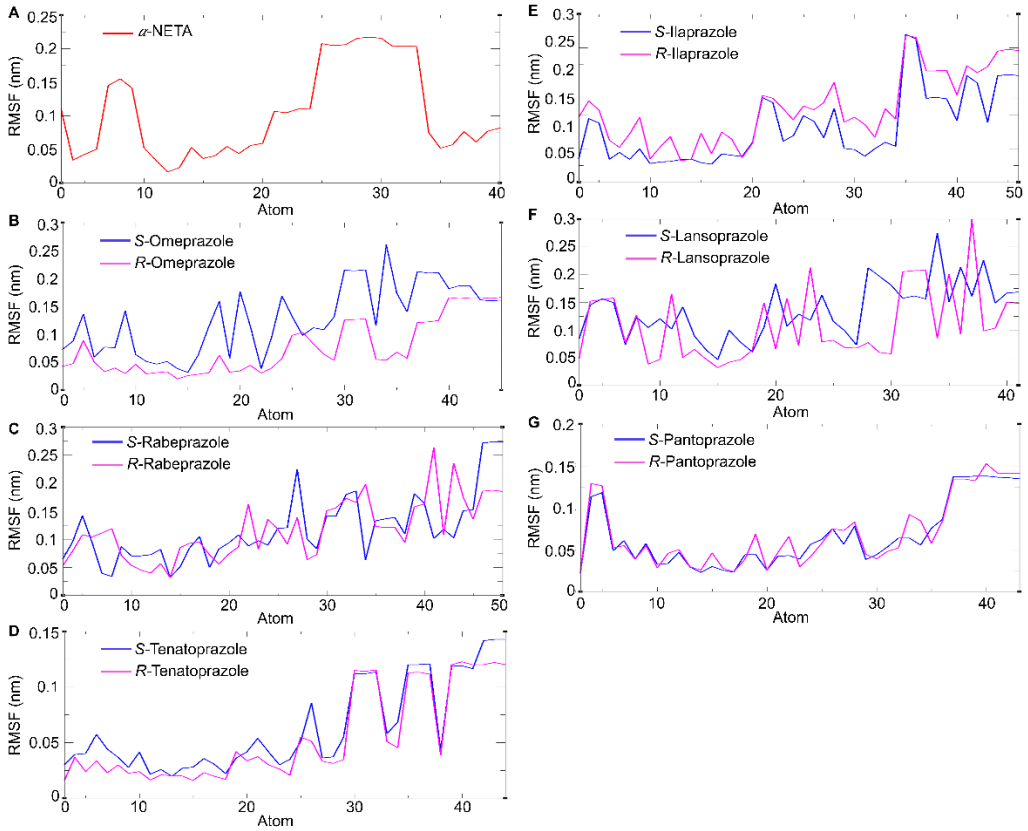

Figure 3.8. RMSF analysis was performed for the *α*-NETA and PPIs as a function of individual atom of the 200 ns trajectory obtained from molecular dynamics simulation in order to measure the average deviation of the atoms over the time from a reference position. A) Represents the RMSF plot of *α*-NETA (red), B) Shows the RMSF plot of *S*-Omeprazole (blue) and *R*-Omeprazole (pink), C) Shows the RMSF plot of *S*-Rabeprazole (blue) and *R*-Rabeprazole (pink), D) Shows the RMSF plot of *S*-Tenatoprazole (blue) and *R*-Tenatoprazole (pink). E) Shows the RMSF plot of *S*-Ilaprazole (blue) and *R*-Ilaprazole (pink). F) Shows the RMSF plot of *S*-Lansoprazole (blue) and *R*-Lansoprazole (pink). G) Shows the RMSF plot of *S*-Pantoprazole (blue) and *R*-Pantoprazole (pink).

The radius of gyration (RoG) measures the distribution of the atoms of the protein around the geometrical space. Results from calculations of this quantity for the ChAT−PPI complexes are depicted in (**Figure 3.9**), to further investigate the compactness of the structure and to measure the extent of the PPIs as it is directly related to the rate of folding of the protein. A relatively stable and low Rg value of within 2.5−2.6 nm was observed for the simulated complexes and explains that the system well retains its three-dimensional quaternary geometrical proportions without any abrupt blow up in the system during the simulation period. The RoG value is one of the most prominent structure activity functions of a macromolecule, as when the ligand forms a complex with the protein there are various conformational changes that take place which ultimately lead to changes in the radius of gyration. (19)

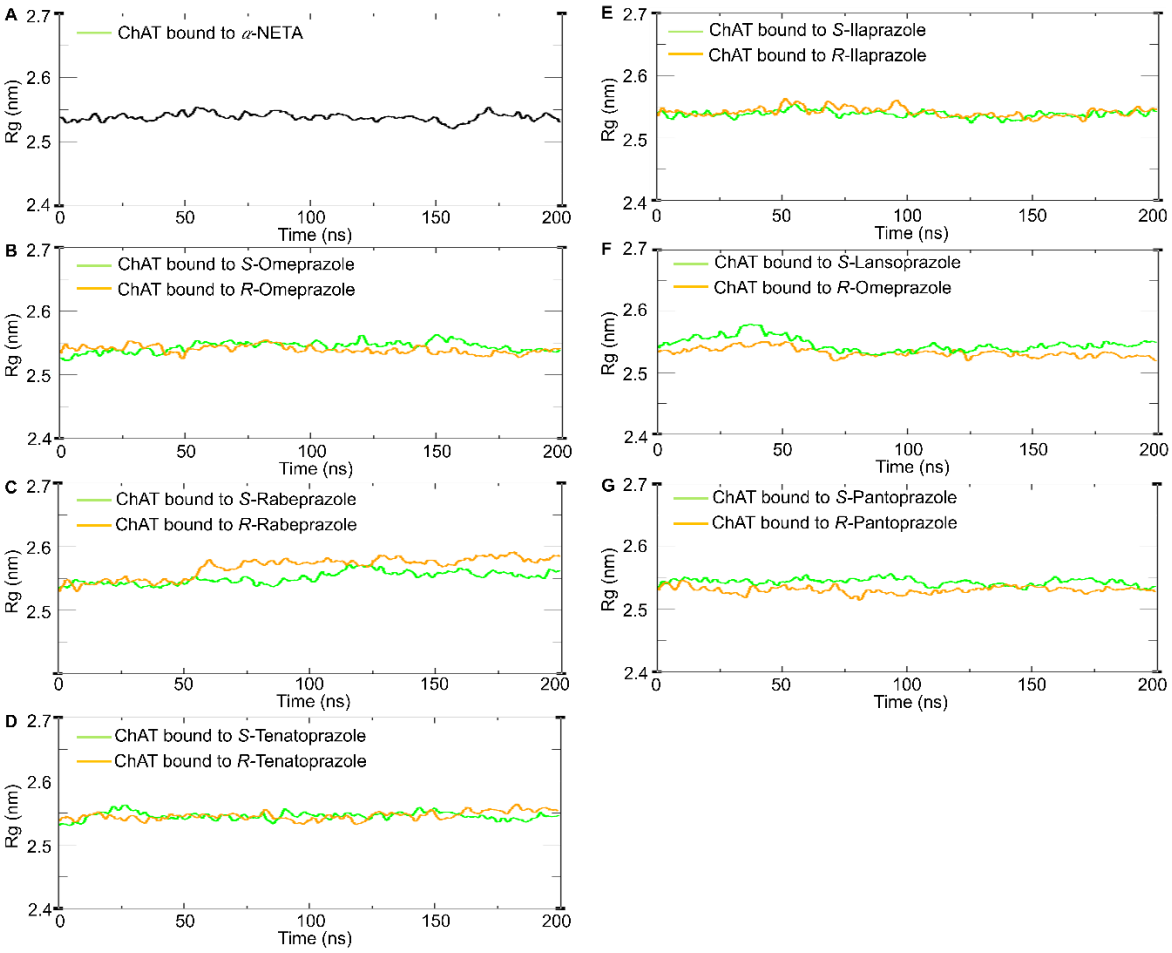

Figure 3.9. RoG analysis was performed for the α-NETA and PPIs complexed with ChAT.

A) Represents the Rg plot of ChAT (black) bound to α-NETA, B) Shows the Rg plot of ChAT bound to *S*-Omeprazole (green) and to *R*-Omeprazole (orange), C) Shows the Rg plot of ChAT bound to *S*-Rabeprazole (green) and to *R*-Rabeprazole (orange), D) Shows the Rg plot of ChAT bound to *S*-Tenatoprazole (green) and to *R*-Tenatoprazole (orange). E) Shows the Rg plot of ChAT bound to *S*-Ilaprazole (green) and to *R*-Ilaprazole (orange). F) Shows the Rg plot of ChAT bound to *S*-Lansoprazole (green) and to *R*-Lansoprazole (orange). G) Shows the Rg plot of ChAT bound to *S*-Pantoprazole (green) and to *R*-Pantoprazole (orange).

Hydrogen bonds are generally considered to be the primary initiators of protein−ligand binding and to be helping in the stabilization of the formed complex. Therefore, a hydrogen bond analysis can make it possible to explore the protein− ligand binding process by analyzing the geometrical positions at each time frame and thereby measuring the number of H-bonds throughout the simulation. The typical optimal distance for a hydrogen bond donor and acceptor is ≤3.5 Å (0.35 nm) with an angle of 180° ± 30°. Thus, we investigated here the average number of hydrogen bonds formed in the ChAT−PPI interactions during the 200 ns dynamic simulation time with a cutoff value of 0.35 nm (**Figure 3.10**). For the classical ChAT inhibitor, α-NETA, there was negligible H-bonding in the first 50 ns of the trajectory (**Figure 3.10A**); thereafter it displayed an average of one H-bond with up to three H-bonds over time. However, the number of H-bonds within 0.35 nm was observed to be maintained for a very limited time period during the simulation as compared with the PPIs. For the latter, the number of hydrogen bonds were maintained in the range of 1 to 8 throughout the simulation period, which suggests that H-bonding played a major role in their interaction and complex formation with ChAT. In addition, the number of H-bonds within the 0.35 nm cutoff is closer to the overall hydrogen bond count (1 to 5 throughout the simulation).

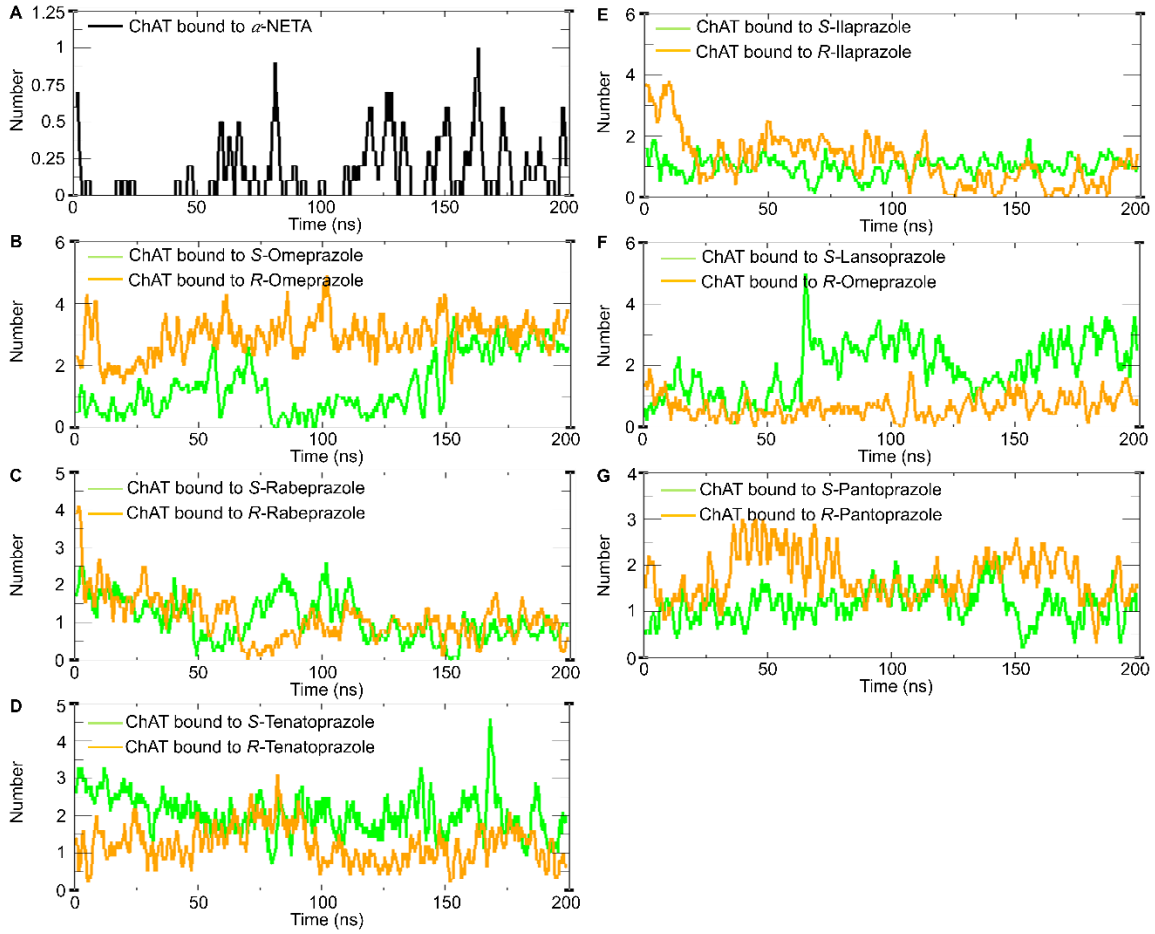

Figure 3.10. Hydrogen Bond Number (HBN) analysis of ChAT's ligands during 200 ns molecular dynamics simulation. A) Shows the HBN plot for α-NETA as the reference ChAT inhibitor (black), B) Shows the corresponding HBN plots for *S*-and *R*-Omeprazole with ChAT (green and orange respectively)**,** C) Shows the HBN plots for *S*-and *R*-Rabeprazole with ChAT (green and orange respectively), D) Shows the corresponding HBN plots for *S*-and *R*-Tenatoprazole with ChAT (green and orange respectively). E) Shows the HBN plot of *S*- and *R*-Ilaprazole with ChAT (green and orange respectively). F) Shows the HBN plot of *S*- and *R*-Lansoprazole with ChAT (green and orange respectively), G) Shows the HBN plot of *S*- and *R*-Pantoprazole with ChAT (green and orange respectively).

To get insight into the hydrophobic core stability of the ChAT protein structure, we analyzed the trajectories for the solvent accessible surface area (SASA) that measures the surface area of the protein that is accessible to or is in contact with the solvent (biofluids). It is a crucial

parameter to be considered since the nonpolar amino acids corroborate the stability of the globular protein in solvent media by shielding the nonpolar amino acid residues inside the hydrophobic core of the protein so isolating them from the aqueous environment. (20, 21) In other words, SASA provides insight into the changes in the compactness of the protein structure as it becomes more accessible to the solvent, which is reflected as an increase in fluctuation in the protein structure. The recorded SASA values varied within 240−280 nm2 (**Figure 3.11 and 3.12**). The findings indicate that the ChAT−PPI complexes are stable as there was only a slight decrease in the SASA value due to the compact conformation of the complex attained toward the end of the simulation. The stability is also reflected by the radius of gyration values. The formed complexes of ChAT−PPIs showed relatively lower SASA as compared to the ChAT protein alone. This seems to be pointing at slight conformational changes that could occur upon the interaction of PPI with the ChAT at an active binding site, which might result in additional shielding of the hydrophobic core accessible to the solvent.

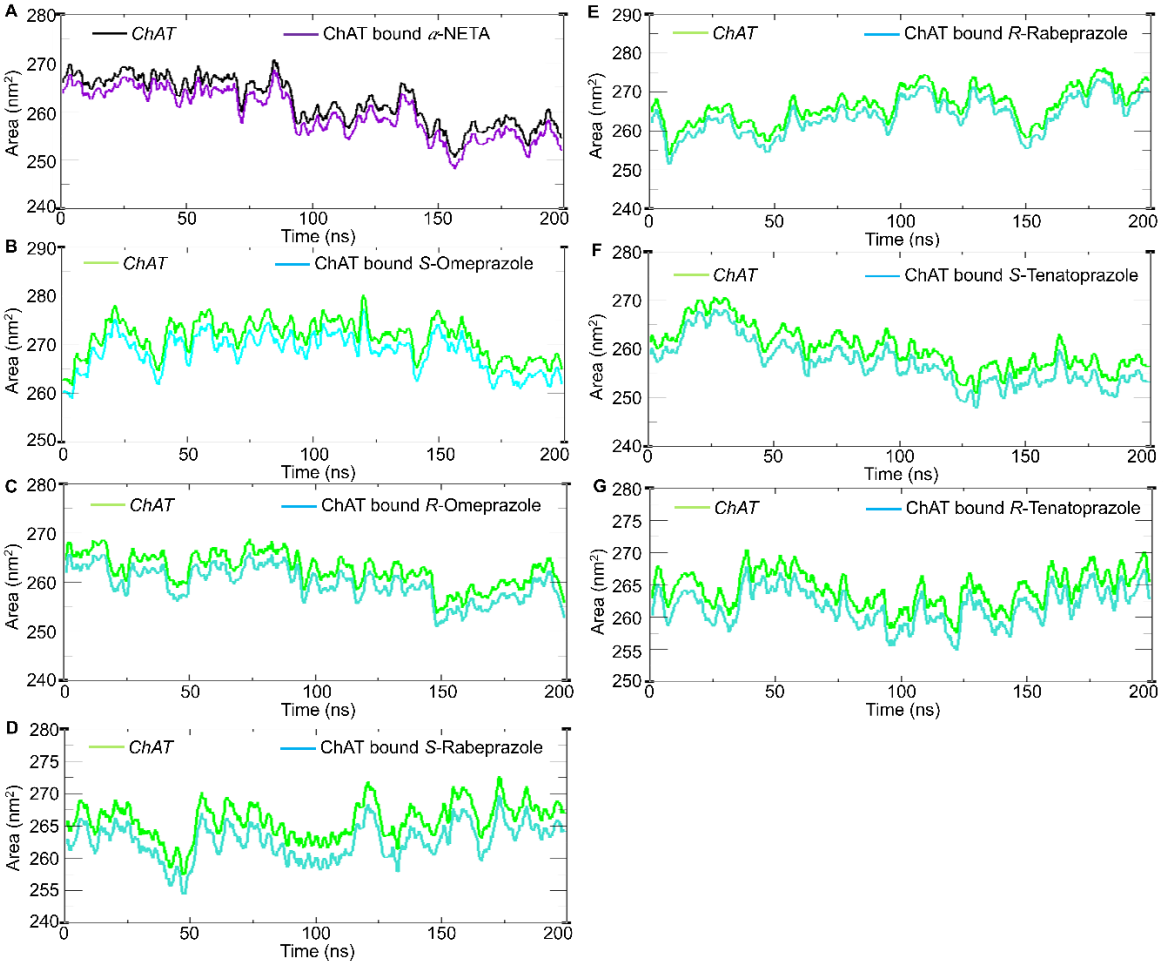

Figure 3.11. Solvent Accessible Surface Area (SASA) analysis of the ChAT protein and ChAT-PPI complexes. A) Represents the SASA plot of ChAT (black) and ChAT-α-NETA complex (magenta), B) Shows the SASA plot of ChAT (green) and ChAT-*S*-Omeprazole complex (sky blue), C) Shows the SASA plot of ChAT (green) and ChAT-*R*-Omeprazole complex (sky blue). D) Shows the SASA plot of ChAT (green) and ChAT-*S*-Rabeprazole complex (sky blue), E) Shows the SASA plot of ChAT (green) and ChAT-*R*-Rabeprazole complex (sky blue), F) Shows the SASA plot of ChAT (green) and ChAT-*S*-Tenatoprazole complex (sky blue), G) Shows the SASA plot of ChAT (green) and ChAT-*R*-Tenatoprazole complex (sky blue). Note that there is a slight decrease in SASA values as the simulation progresses, which indicates a stable complex formation as the system becomes compact and as the protein surface that is accessible to the solvent is decreased.

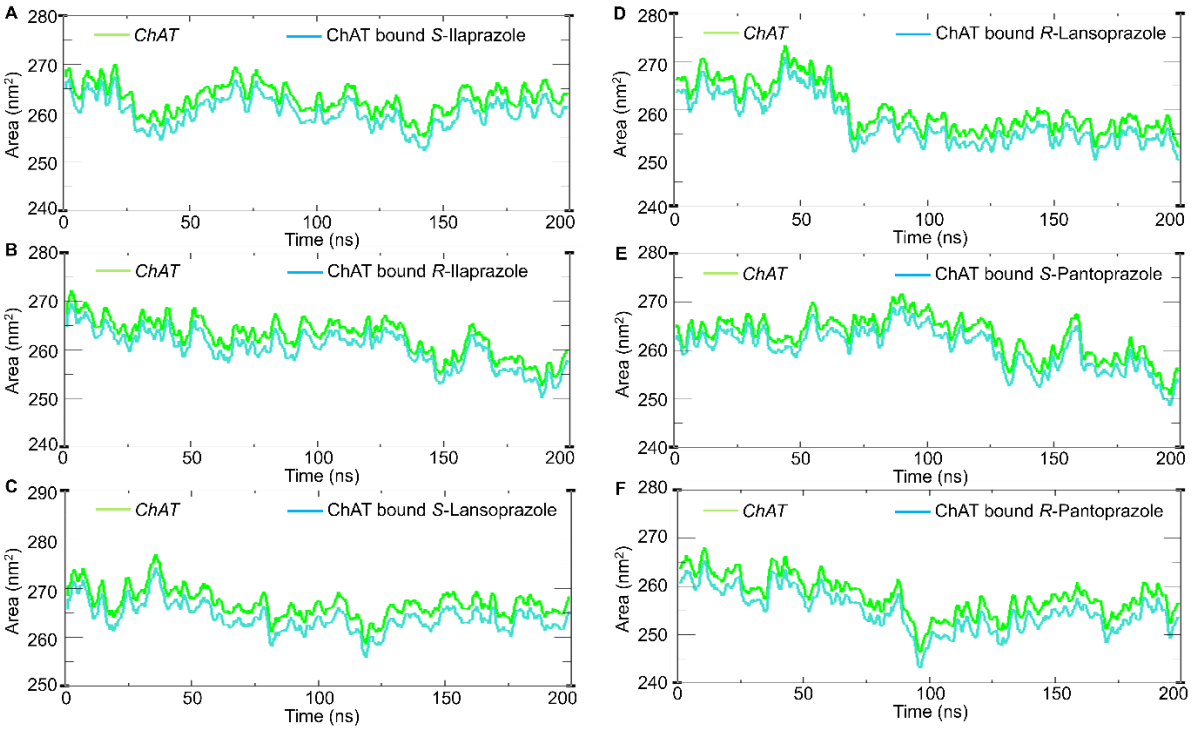

Figure 3.12. SASA of the ChAT protein and ChAT-PPI complex. A) Shows the SASA plot of ChAT (green) and ChAT-*S*-Ilaprazole complex (sky blue) B) Shows the SASA plot of ChAT (green) and ChAT-*R*-Ilaprazole complex (sky blue). C) Shows the SASA plot of ChAT (green) and ChAT-*S*-Lansoprazole complex (sky blue) D) Shows the SASA plot of ChAT (green) and ChAT-*R*-Lansoprazole complex (sky blue). E) Shows the SASA plot of ChAT (green) and ChAT-*S*-Pantoprazole complex (sky blue) F) Shows the SASA plot of ChAT (green) and ChAT-*R*-Pantoprazole complex (sky blue). Note that there is a slight decrease in SASA values as the simulation progresses, which indicates a stable complex formation as the system becomes compact and as the protein surface that is accessible to the solvent is decreased.

3.3.2.1. Principal Component Analysis

We also performed a principal component analysis (PCA) for the simulated systems. PCA is also known as “essential dynamics” and can identify the most crucial conformational degrees of freedom of the simulated system based on the principles of covariance matrix. PCA allows identifying the principal components that together explain the overall motions of the protein.

This reduction in the data is derived by the linear transformation of the original variables to a set of new concerted variables, which allows one to interpret the features of the data set from only few "principal components" (22). The eigenvalues of the first 10 principal components (eigenvectors) for the ligand−ChAT complexes are shown in (**Figure 3.13 and 3.14**).

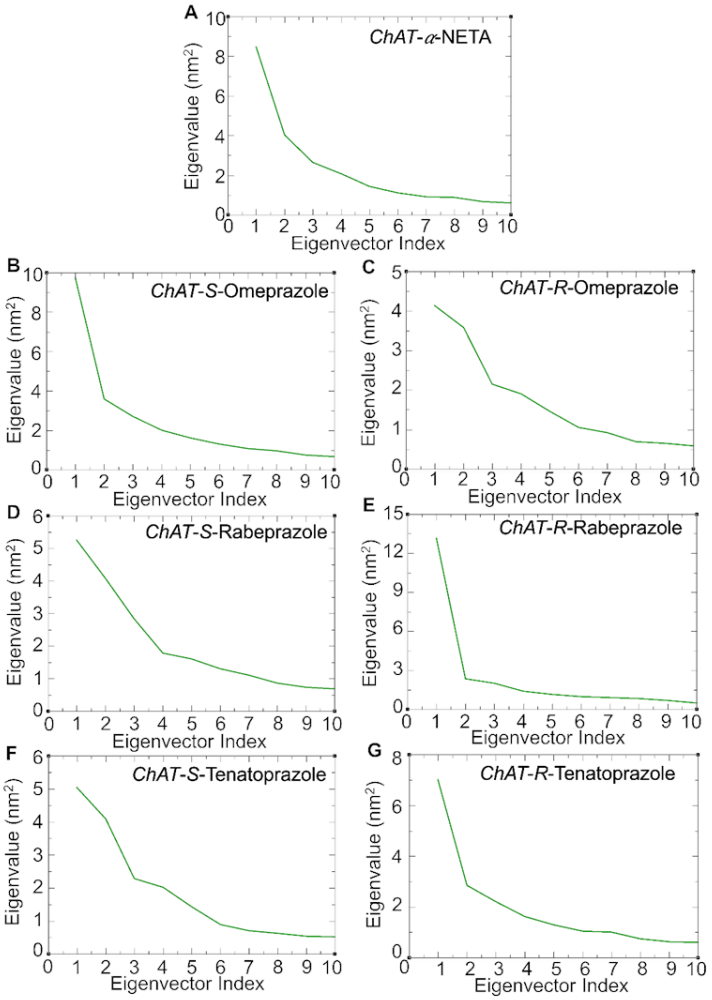

Figure 3.13. The eigenvalues of the first 10 principal components of the simulated system for the ChAT-ligand complexes. Here, the principal component analysis identifies the most contributing parameters that explain the structural stability of ChAT during its interaction with the ligands. The plot suggests that the first two PC eigenvectors account for the maximum of the motions in the system.

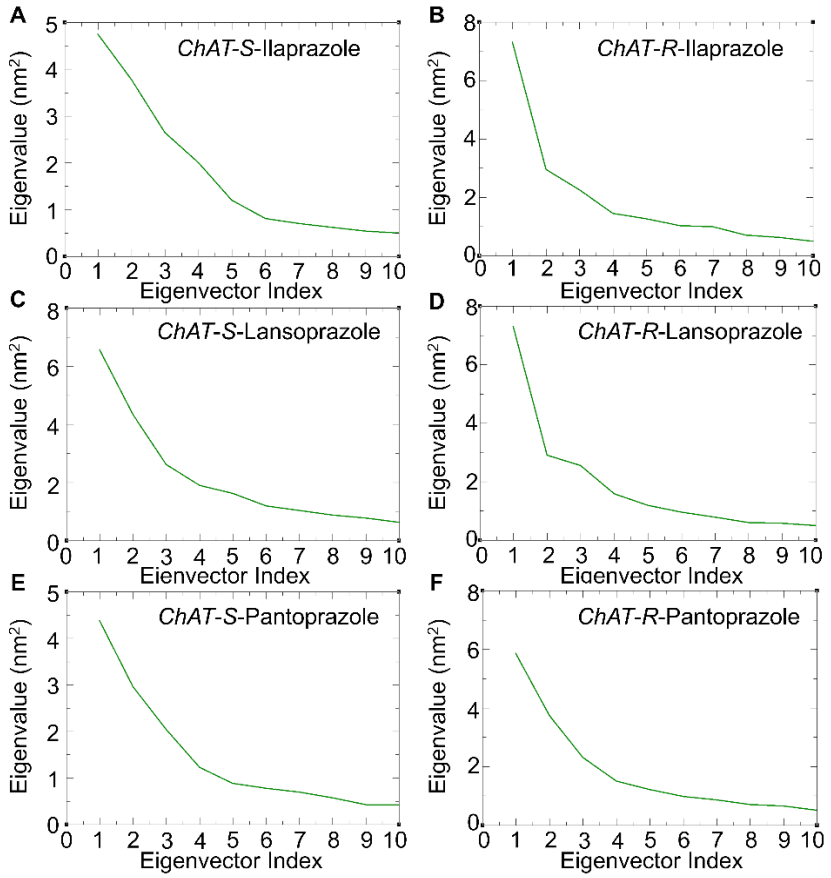

Figure 3.14. Representation of the eigenvalues of the first 10 principal components for all the ChAT-PPI complex simulated system. Principal component analysis tries to find a combination of features that can explain the maximum separation and distinguish between the data points. The plot suggests that the first two PC eigenvectors accounts for maximum of the motions in the system.

These analyses showed that the first four components explained most of the variations in the data. This was 51.5% for α-NETA, i.e., the reference ChAT inhibitor, 48.1% for *S*-Ilaprazole, 48.8% for *R*-Ilaprazole, 47.8% for *S*-Lansoprazole, 49.9% for *R*-Lansoprazole, 50.5% for *S*-Omeprazole, 43.2% *R*-Omeprazole, 47.5% *S*-Pantoprazole, 45.4% *R*-Pantoprazole, 45.3% *S*-Rabeprazole, 55.8% for *R*-Rrabeprazole, 49.1% for *S*-Tenatoprazole, and 46.9% for *R*-tenatoprazole. Then, the first two most important principal components were used to plot the 2D PCA projection (**Figure 3.15**). The PCA graph shows the various conformational changes that occurred in the ChAT protein structure during the course of simulation. The 2D plot shows

widespread distribution in the conformational space with stable clusters, most likely due to various conformational changes in the protein quaternary structure upon molecular interaction with the PPIs, resulting in various stable conformational states.

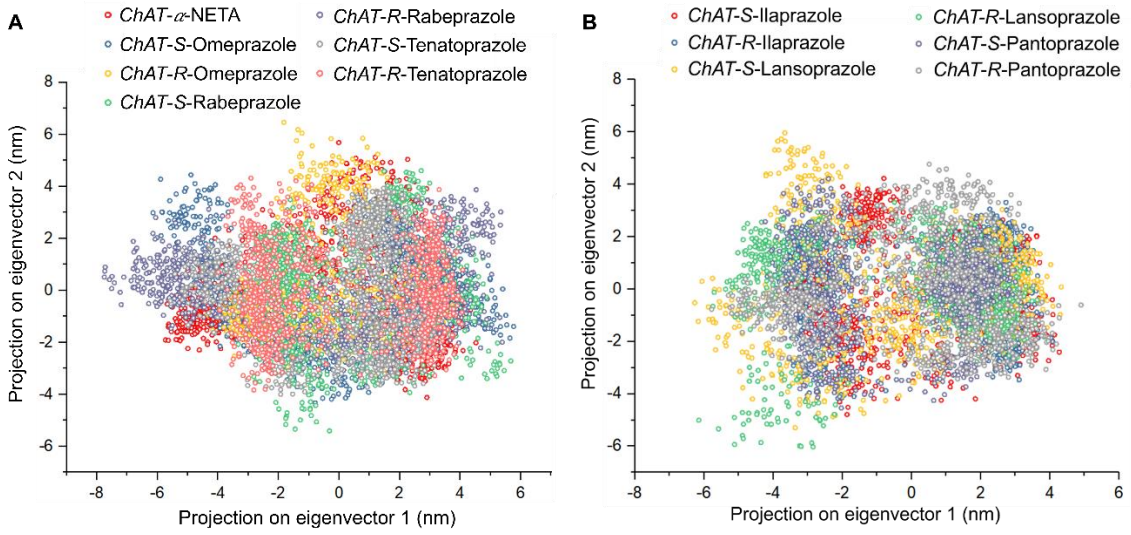

Figure 3.15. The 2D projection of the first two principal components for the ChAT-ligand complex system. Each dot on the plot is a representation of a specific conformational state in the ChAT protein with the ligands, i.e., α-NETA and the specified PPIs throughout the simulation. The spread represents the primary conformational changes in the ChAT protein during the interaction of ChAT with PPIs throughout the time span of the simulation. Overall, the graph represents a uniform widespread distribution of the conformational sampling for all the complexes.

3.3.2.2. Free-Energy Landscape Analysis

The free-energy landscape (FEL) analysis implements two variables that can directly reflect the specific properties of the system, namely the changes in the RMSD of the system versus the RoG. The FEL analysis therefore measures the stability of the conformational changes in relation to changes in the Gibbs free energy (ΔG) of the system. FEL analysis holds the essential key to the unraveling various biochemical processes (23). We hence assessed the energy minima landscape for the various ChAT−ligand complexes (**Figure 3.16 and 3.17**), and the

shape and size of the energy minima landscapes were investigated. The color code bars in these figures provide information about the energy levels of the complexes during the simulation. For instance, in the 2D energy landscape, the centralized blue areas show the complex within the cluster with the least energy and hence the most stability. In the 3D projections, the narrow-shaped funnel illustrates the dynamic changes in conformations with respect to time for the system to reach a stable structure with the lowest energy.

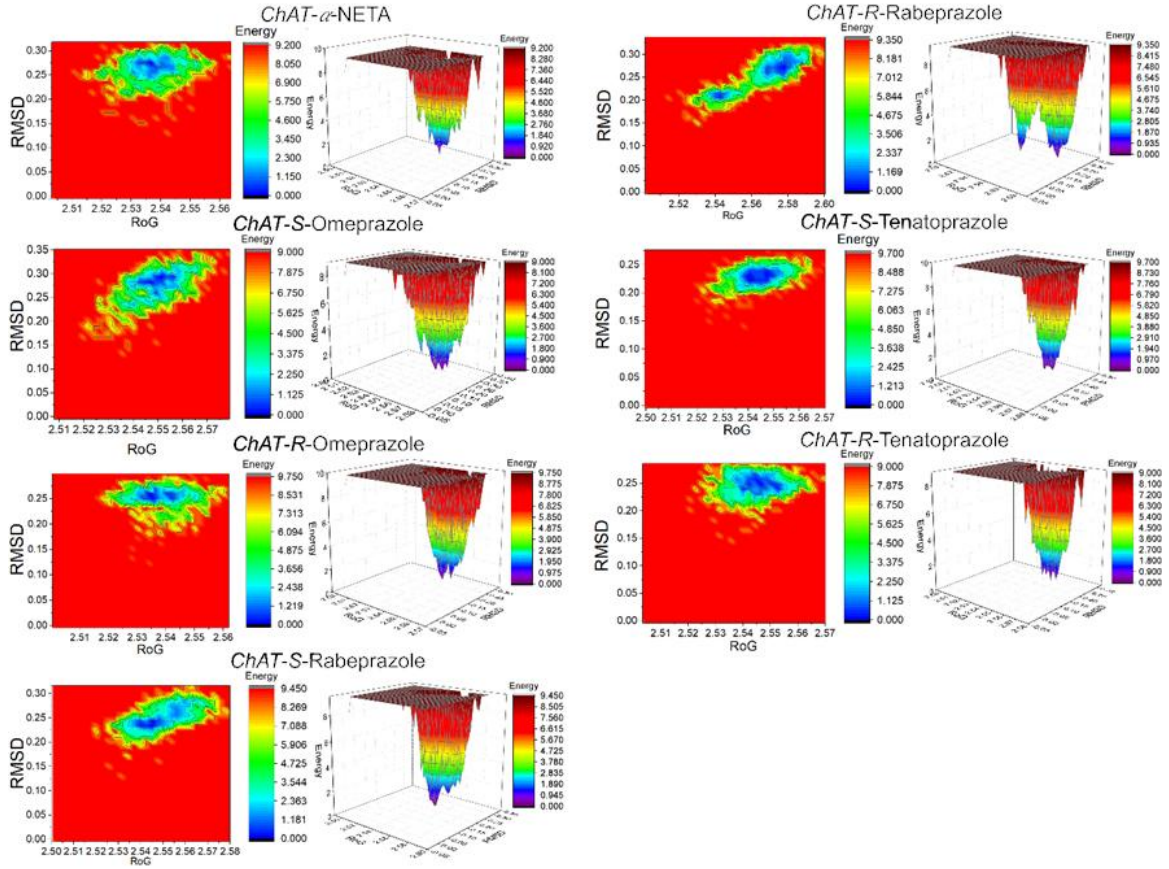

Figure 3.16. The 2D and 3D free energy landscape diagram as a function of RMSD and Rog as the two coordinates that depict the folding of ChAT- during its interaction with αNETA versus the stereoisomers of PPIs. The free energy is displayed in terms of kJ/mol in the indicated color codes where the purple color represents least energy and red the highest energy. The simulated folding of the protein-ligand complex system forms a distinct narrow funnel that ultimately denotes a stable folding state with lowest energy minima, and thereby highest stability. The 2D contour plots and the 3D projections were plotted using the OriginPro

2017 software (OriginLab Inc., Northampton, MA, USA). RMSD= Root mean square deviation; RoG = radius of gyration of the system.

The FEL analysis revealed that the ΔG values of the ChAT− ligand complexes converge to an energy minimum state which is illustrated in the overall 3D plots as a single funnel formed for the ChAT complexes with α-NETA and the PPIs (**Figure 3.16 and 3.17**). This along with the 2D contour plot clearly illustrates that in the simulated system all the ChAT−PPI complexes reached a single distinct local energy minimum and hence a stable folding state. However, an exception was observed for the ChAT−*R*-Rabeprazole system (**Figure 3.16**) where the 3D plot shows two distinct local energy minima, indicating that *R*-Rabeprazole might induce two different geometrical conformations and relatively stable folding states during its interaction with ChAT.

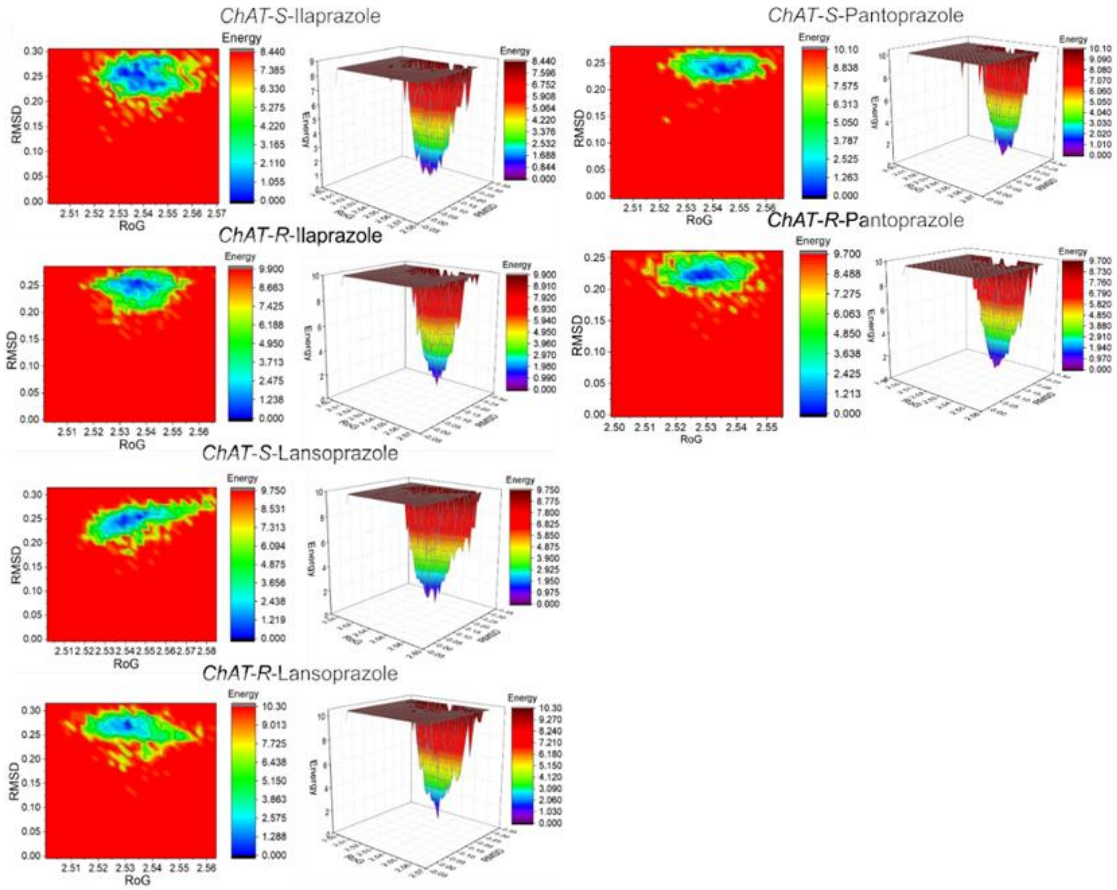

Figure 3.17. The 2D and 3D free energy landscape diagram as a function of RMSD and Rog as the two coordinates that depict the folding of ChAT- during its interaction with

αNETA versus the stereoisomers of PPIs. The free energy is displayed in terms of kJ/mol in the indicated color codes where the purple color represents least energy and red the highest energy. The simulated folding of the protein-ligand complex system forms a distinct narrow funnel that ultimately denotes a stable folding state with lowest energy minima, and thereby highest stability. The 2D contour plots and the 3D projections were plotted using the OriginPro 2017 software (OriginLab Inc., Northampton, MA, USA). RMSD= Root mean square deviation; RoG= radius of gyration of the system.

3.3.3. Residue Interaction Network (RIN) Analysis

RIN analysis has been extensively applied for the analysis of mutation effects, protein folding, domain−domain communication, and catalytic activity of enzymes. The network interaction analysis diagrams for ChAT and the ligands are shown in (**Figure 3.18 and 3.19**). The analyses indicate that the HIS324 is the most important amino acid residue in the ChAT catalytic tunnel for its interaction with most of the PPIs. Given that HIS324 governs the catalytic nucleophilic attack on acetylcholine or acetyl-CoA (depending on the direction of the enzyme reaction), the finding suggests that PPIs might inhibit ChAT by blocking HIS324. Nonetheless, no HIS324 residue interaction is apparent for the R-omeprazole and S-pantoprazole in the energy minima complexes.

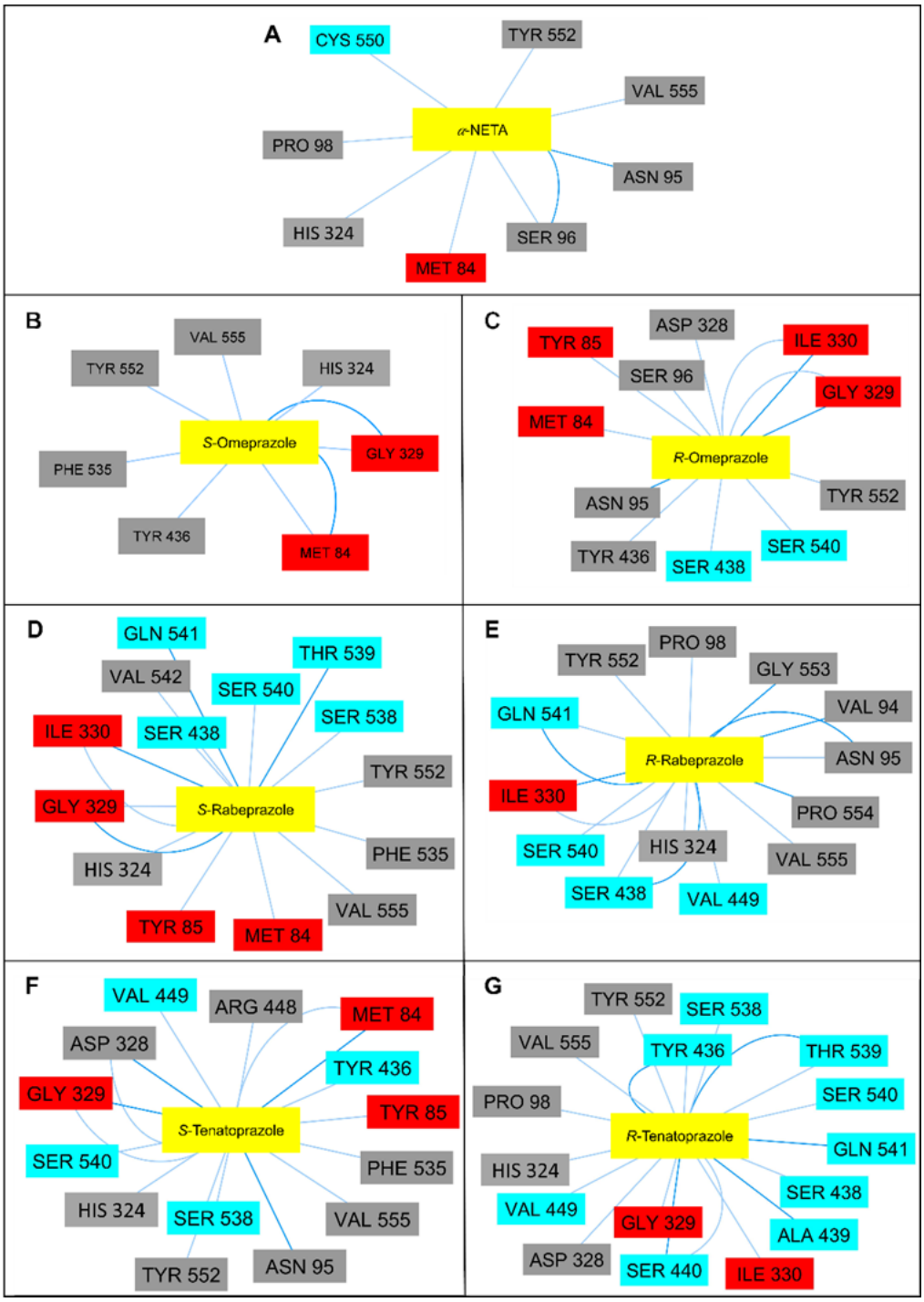

Figure 3.18. The Residue Interaction Network Analysis for α-NETA versus the stereoisomers of Omeprazole with ChAT. The specific ligand is highlighted in yellow at the center together with the interacting amino acid residue. The color code denotes the amino acid residue as part of a certain secondary structure in the ChAT protein as follows: red color = the alpha helices, blue =the beta sheets, and grey= the loops in the ChAT protein structure.

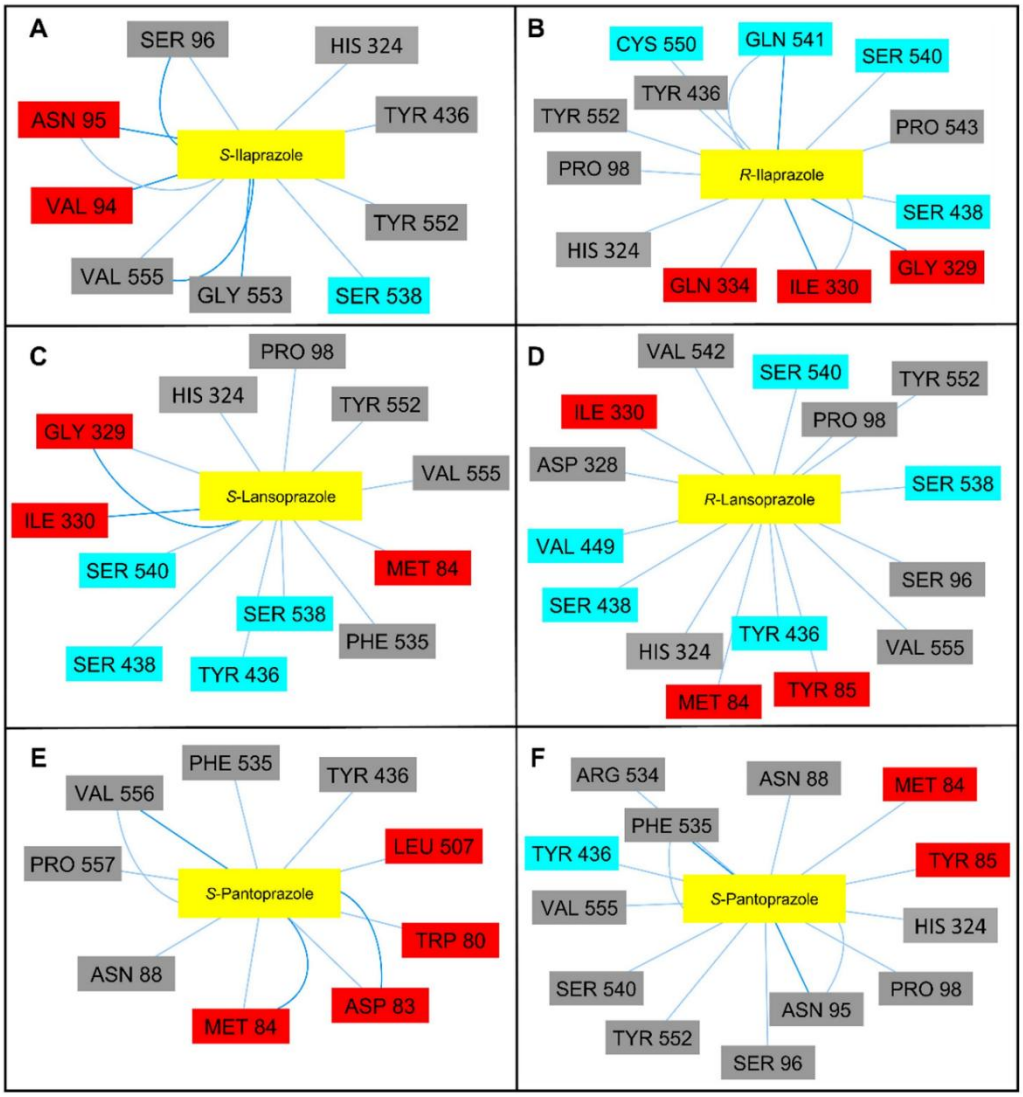

Figure 3.19. Residue Interaction Network (RIN) Analysis of PPIs with ChAT. The PPI is highlighted in yellow at the center and the amino acid residues interacting are shown where the red color denotes the alpha helices, sky color represents the beta sheets, and grey color indicates the loops.

3.3.4. Molecular Mechanics Poisson−Boltzmann Surface Area (MM-PBSA) Analysis

To estimate the molecular binding interaction of the PPIs in the active binding pocket of the ChAT protein, we calculated the binding free energy (ΔG) using MM-PBSA (**Figure 3.20**). These calculations include the energetic terms for van der Waals contributions from molecular mechanics, the electrostatic energy and the electrostatic contribution to the solvation free

energy calculated by the Generalized Born equation, and the nonpolar contribution to the solvation free energy calculated by an empirical model (24). To assess the Gibbs binding free energy along the simulation, we initially performed an MM-PBSA calculation on the lowest energy minima frame of the simulation trajectory and two of its adjacent frames; the resultant ΔG was then taken as an average of the three frames. These data are presented in **Table 3.2**.

Table 3.2. MM-PBSA binding free energy (ΔG) calculations for PPIs with ChAT.

	PPI	**van der Waals**	**Electrostatic energy**	**EGB**	**ESURF**	**GGAS**	**GSOLV**	**Averaged ΔG (kcal/mol)**
1	α-NETA	-30.95	-29.84	41.34	-4.14	-60.79	37.20	-23.58
2	*S*-Ilaprazole	-39.85	-18.77	41.54	-4.74	-58.62	36.79	-21.82
3	*R*-Ilaprazole	-43.51	-22.65	46.02	-5.28	-66.16	40.74	-25.42
4	*S*-Lansoprazole	-40.28	-18.01	41.62	-6.1	-58.29	35.52	-22.77
5	*R*-Lansoprazole	-40.19	-38.96	49.16	-6.31	-79.15	42.85	-36.29
6	*S*-Omeprazole	-42.08	-6.48	29.04	-5.37	-48.57	23.67	-24.89
7	*R*-Omeprazole	-39.94	-21.51	44.97	-5.39	-61.46	39.58	-21.87
8	*S*-Pantoprazole	-35.89	-30.99	50.24	-5.15	-66.88	45.08	-21.80
9	*R*-Pantoprazole	-43.63	-20.07	43.93	-6.36	-63.70	37.57	-26.13
10	*S*-Rabeprazole	-42.65	-32.81	55.83	-6.42	-75.46	49.41	-26.05
11	*R*-Rabeprazole	-39.16	-23.45	47.73	-6.01	-62.61	41.71	-20.90
12	*S*-Tenatoprazole	-46.60	-24.56	42.47	-6.55	-71.16	35.92	-35.23
13	*R*-Tenatoprazole	-46.86	-28.62	48.90	-6.41	-75.48	42.48	-33.00

MM-PBSA= Molecular mechanics Poisson–Boltzmann surface area; EGB= the electrostatic contribution to the solvation free energy calculated by PB or GB; ESURF= nonpolar contribution to the solvation free energy calculated by an empirical model; GGAS= Gibbs free energy into a gas-phase term; GSOLV= Gibbs free energy into a solvation term.

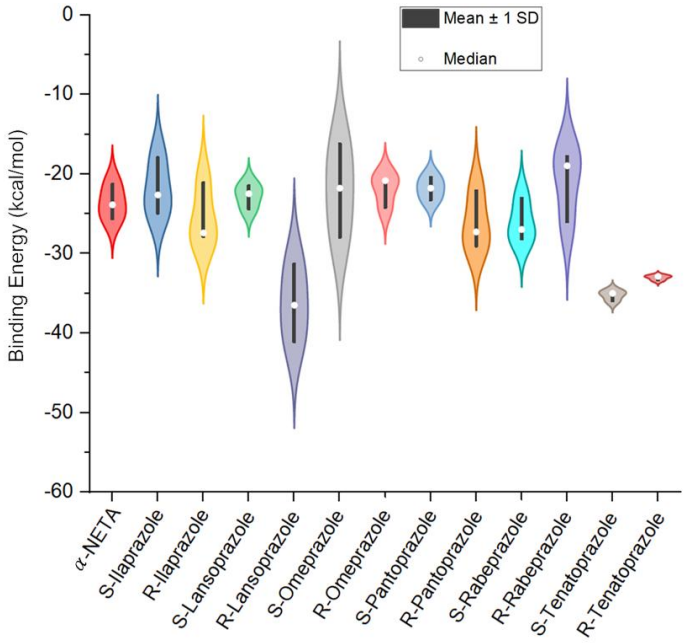

Figure 3.20. Violin plot for the *in silico* calculated ΔG binding free energies, (kcal/mol) by MM-PBSA. Binding energies were evaluated for the lowest energy minima frame of the simulation trajectory and two of its adjacent frames. A Violin plot is a hybrid plot comprising of the box plot and a kernel density plot that show peaks in the data. It can depict the summary statistics and the density of each variable. The mean is shown as the average of the total data with a standard deviation of ± 1 denoted by the thick black vertical bar in the center and the median denoted by the white circle is the exact middle value in the dataset.

A closer look at the individual contributions of each component for the overall binding ΔG suggests that the van der Waals, the electrostatic energy, and the nonpolar contribution to the solvation free energy (ENSURF) positively contributed to the overall binding interaction, whereas the electrostatic contribution to the solvation free energy seems to exert a negative contribution (**Table 3.2; Figure 3.21 and 3.22**). Noteworthy, these MM-PBSA results indicate that *R*-Lansoprazole has the best binding with a ΔG score of −36.29 kcal/mol, which may be because of the methylene group of the trifluoro ethoxy substitution present at the fourth position of the pyridine ring undergoing an alkyl−alkyl interaction with the VAL555 amino acid residue

as well as because the π-electrons of the pyridine ring form π-alkyl interactions with the HIS324 and SER540 amino acids. *S*-Tenatoprazole and *R*-tenatoprazole follow with the next highest MM-PBSA scores of −35.23 and −33.00 kcal/mol respectively (**Table 3.2 and Figure 3.20**).

As explained in the foregoing and the present analysis, the use of well-established docking algorithms and MD force fields constitutes yet another step toward the understanding of the mechanism of PPI−ChAT binding (25, 26). We can here foresee overcoming present limitations in the analysis and better distinguishing the ligands by combining binding energy data with dynamical data, e.g., by using umbrella sampling type MD to predict so-called k_{on} and k_{off} quantities (26, 27). This tells how the ligand can overcome intermediate energy barriers to reach the final poses of interaction and thereby also makes it possible to predict the residence time in these poses. A way to reach further propagation time is to apply the meta dynamics concept where the selection of collective variables enables the study of much longer time sequences and finding also more of the "hidden" binding sites with smaller binding strengths (28). Such development in the analysis must of course be qualified with respect to the steep increase in computer time it brings about.

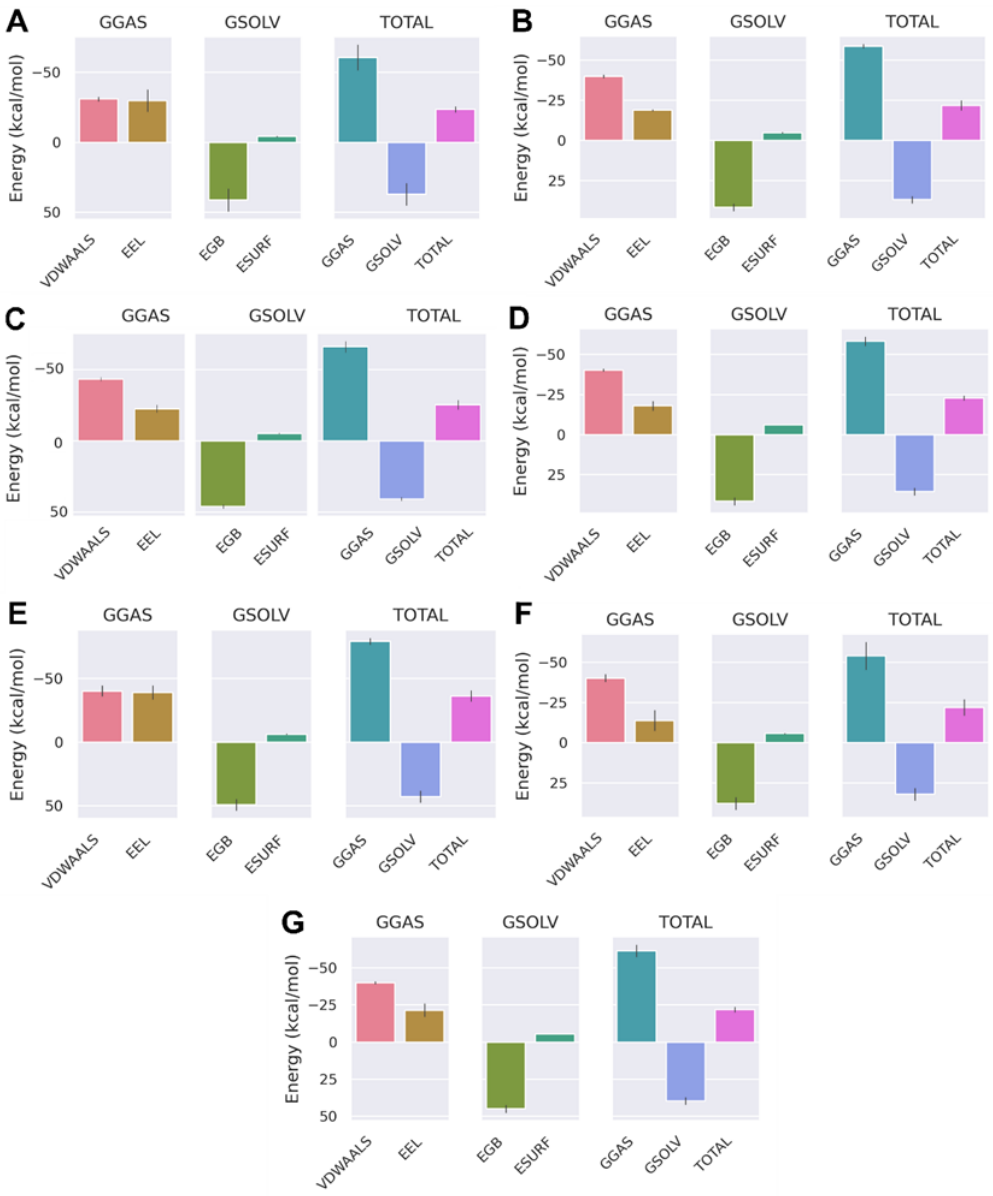

Figure 3.21. In silico calculated Binding Free Energy (Kcal/mol) ΔG by MM-PBSA. A) Represents the ΔG for ChAT-*α*-NETA complex. B) Shows the ΔG for ChAT-*S*-Ilaprazole. C) Shows the ΔG for ChAT-*R*-Ilaprazole. D) Shows the ΔG for ChAT-*S*-Lansoprazole. E) Shows the ΔG for ChAT-*R*-Lansoprazole. F) Shows the ΔG for ChAT-*S*-Omeprazole. G) Shows the ΔG for ChAT-*R*-Omeprazole

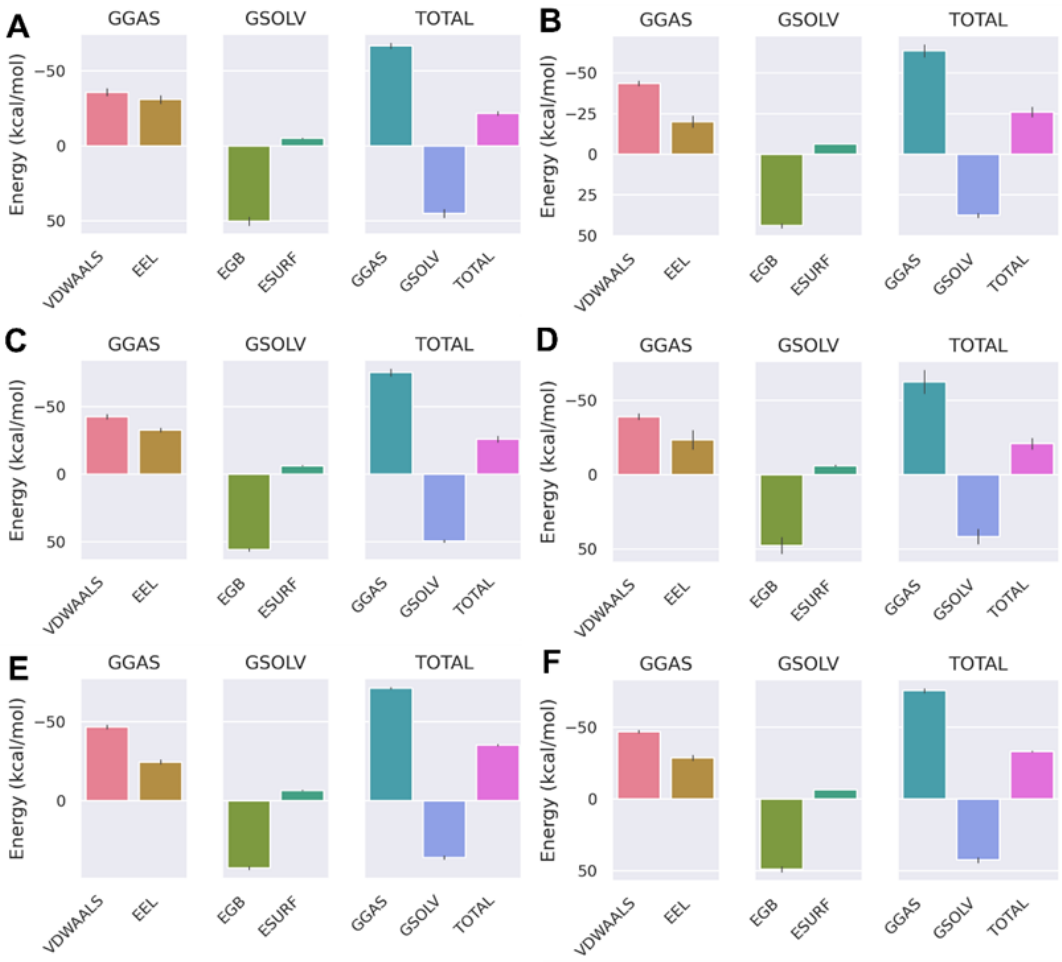

Figure 3.22. In silico calculated Binding Free Energy (Kcal/mol) ΔG by MM-PBSA. A) Represents the ΔG for ChAT-*S*-Pantoprazole. B) Shows the ΔG for ChAT- *R*-Pantoprazole. C) Shows the ΔG for ChAT-*S*-Rabeprazole. D) Shows the ΔG for ChAT-*R*-Rabeprazole. E) Shows the ΔG for ChAT-*S*-Tenatoprazole. F) Shows the ΔG for ChAT-*R*-Tenatoprazole.

3.3.5. In Silico BBB Permeability Analysis

For CNS drug discovery, blood−brain barrier permeability is one of the primary requisites to be considered from the early phase of development as it is the physiological barrier that regulates the permeability of xenobiotics into the brain. The BBB permeability of the PPIs was estimated using the CBligand Web server (https://www.cbligand.org/BBB/predictor.php) (29). All the PPIs were predicted to be BBB permeable, and the results are given in **Table 3.3** (SVM_MACCSFP BBB Score >0.02 are able to cross the BBB) where tenatoprazole, omeprazole, and rabeprazole were the top three in crossing the BBB, with scores of 0.134,

0.124, and 0.123, respectively. Moreover, literature reports suggest that PPIs can cause adverse neurological effects, mainly headaches, (30) and in vivo animal studies demonstrate that about 15% of the total intravenous dose can reach the central nervous system and can potentially affect the cognitive functions (31) indicating the BBB permeability of the PPIs in humans. It is one of the prime concerns, especially for the geriatric population, that the blood−brain barrier tends to display some alterations which lead to the loosening of the BBB and the loss of selectivity of passage of some chemicals from blood to the central nervous system (32, 33).

Table 3.3. Predicted in-silico BBB permeability.

Sr. No.	Compound	SVM_MACCSFP BBB Score	BBB (+/-)
1	Ilaprazole	0.101	+
2	Lansoprazole	0.096	+
3	Omeprazole	0.124	+
4	Pantoprazole	0.082	+
5	Rabeprazole	0.123	+
6	Tenatoprazole	0.134	+

3.3.6. Molecular Docking Study

To investigate the precise changes in the binding interactions influenced by the N-Methylation of Tenatoprazole, N-Methyl Tenatoprazole was docked on the ChAT biding cavity to understand the precise binding interactions and changes that could relate to the reduced inhibitory activity on ChAT. **Figure 3.23** The 2D docking interactions of the *S*- and *R*- enantiomers of N-Methyl Tenatoprazole indicate that there is a loss of interaction of the pyridine ring with the HIS324 catalytic residue. On closer inspection of the 3D binding pose (**Figure 3.24**) of the N-Methyl Tenatoprazole by overlapping with the Tenatoprazole it was observed that the loss of activity was due to binding pose was inverted where the pyridine is facing the entrance of the tunnel and does not dig deep enough in the tunnel to interact with the HIS324 and the N-Methylated

4-Azabenzimidazole ring of the N-Methyl Tenatoprazole goes deep into the pocket and does not have interaction with the catalytic residue HIS324.

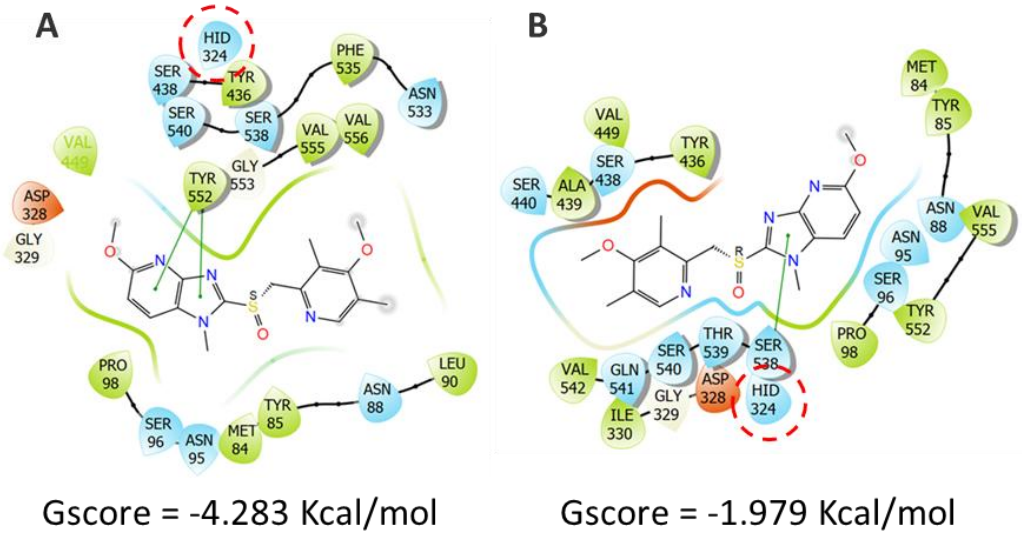

Figure 3.23. Comparison of the selected 2D-docking poses for the stereoisomers of N-methyl Tenatoprazole with ChAT. (A) 2D docking interaction for the stereoisomer N-methyl *S*-Tenatoprazole with ChAT (B) Selected 2D interaction diagram for the stereoisomer N-methyl *R*-Tenatoprazole with ChAT.

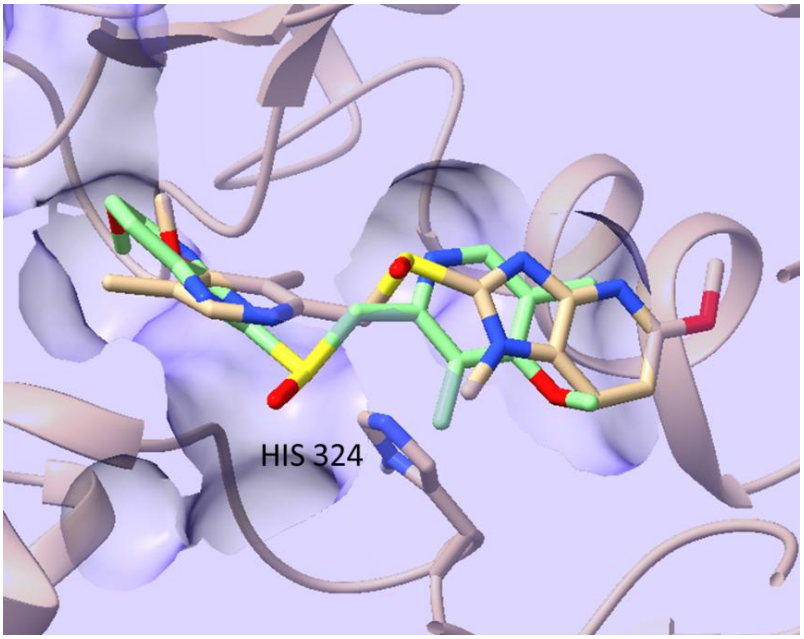

Figure 3.24. 3D comparison diagram of the binding mode of Tenatoprazole vs N-methyl Tenatoprazole in the ChAT binding tunnel.

3.4. Materials and Methods

3.4.1. Molecular Docking Study

To get insight into the probable binding interaction and how PPIs interact with the ChAT protein in the active site, we carried out in silico molecular docking using the Glide module in Schrodinger-Maestro (34) (Schrodinger LLC 2009, USA). Initially, the X-ray crystal structure of the ChAT protein (PDB ID: 2FY3) was downloaded from the RCSB Protein Data Bank and was manually examined for any missing residues. Six different commercially available PPIs, namely, ilaprazole, lansoprazole, omeprazole, pantoprazole, rabeprazole, and tenatoprazole, were chosen for our study. The structures were obtained from PubChem (35) and were further manually investigated for any error. The PPIs were subjected to ligand preparation by the Ligprep wizard in Maestro (Schrodinger). The preprocessing performed many corrections on the PPIs such as the addition of hydrogens, 2D to 3D structure conversion, bond length and bond angle correction, stereochemistry, and ring conformation followed by energy minimization and optimization with the help of the optimized potential for liquid simulations (OPLS 2005) force field (36). Subsequently the R and S enantiomers of the PPIs were generated as it is known that chirality plays a major role in their bioactivity (37).

The ChAT protein X-ray crystal structure (PDB: 2FY3) (38) was subjected to the protein preparation wizard in Maestro (39). The preprocess carried out the correction of raw PDB data, where amendments like the addition of hydrogens, bond order assignment, creation of zero-order bonds to metals, disulfide bond creation, charge fixation, and group orientation were performed. The receptor grid was generated using the receptor grid generation tool in Maestro, where we selected the ligand bound protein X-ray crystal structure, where it identifies the bound ligand molecule in order to exclude it from the grid generation and generates a grid box around the active binding cavity. The scaling factor and partial charge cutoff of van der Waals radius scaling was kept at 0.25 and 1 Å by default, respectively. Other parameters were set at default

settings in Maestro (40).

After ligand preparation, protein preparation, and grid generation, molecular docking was carried out using the Glide module, (41) which uses systematic computational simulation methods for evaluation of the particular binding poses and the ligand flexibility. Extra precision (XP) docking (41) was carried out that gives various favorable binding poses with the GScore module, which provides an empirical scoring function as a combination of different parameters. The best scoring pose showing interaction with the HIS324 residue of the active site was chosen for further analysis.

3.4.2. Molecular Dynamics Simulation

Classical molecular dynamics simulations were further carried out using GROMACS2020 (42) and the CHARMM 36m force field (43) as described earlier (44). Briefly, the top scoring complex obtained from molecular docking showing interaction with the HIS324 residue in the active binding site was used for system input generation using the CHARMM-GUI Web server (45, 46). The complex was solvated using the TIP3P water model (47) and was accommodated in a cubic box of dimension $10 \times 8 \times 8$ nm^3 , and the system was neutralized by adding Na+ and Cl− ions with the help of the Monte Carlo ion placing method (48). The prepared systems were subject to energy minimization using the steepest descent algorithm for 50000 steps until the maximum force became less than 1000 (kJ/mol)/nm, with constraints on H-bonds utilizing the LINCS algorithm, (49, 50) followed by a 2 ns of equilibration step with the help of Nose−Hoover temperature coupling (51) using constant number, volume, and temperature (NVT) at a temperature of 303.15 K. Finally, the system was subject to an isobaric−isothermal (NPT) production simulation run for 200 ns under periodic boundary conditions using the Parrinello−Rahman pressure coupling at 1 atm pressure (52). Finally, the obtained simulation trajectory was further analyzed quantitatively by calculating various parameters like the RMSD, RMSF, RoG, SASA, and free energy landscape diagrams by using gmx_rms, gmx_rmsf,

gmx_gyrate, gmx_sasa, and gmx_sham functionalities, respectively, available in GROMACS. The formation of hydrogen bonds was also analyzed for the ChAT−PPI complex during the 200 ns long trajectory.

PCA also known as essential dynamics was performed for the systems to find the low-dimensional approximations of the most important motions in the protein (53). "Essential dynamics" refers to the subspace comprising only a few degrees of freedom that can explain most of the positional fluctuations whereas the remaining space can be considered as physically constrained. This leaves the essential degrees of motion free that can explain the relevant protein motions (53). We also utilized other modules available in GROMACS, like gmx_covar and gmx_anaeig. PCA was performed on the ChAT−PPI complexes in two steps: (a) building of the covariance matrix by selecting the backbone atoms and (b) diagonalizing the covariance matrix of the atomic coordinates. Finally, the relative motion for the complex was obtained with respect to the projection of the first two eigenvectors that account for the maximum motion of the system

3.4.3. Residue Interaction Network Analysis

To identify the amino acid residues that may play a crucial role in the stabilization of the ChAT−PPI complex formation and reaching the global energy minima, the residue interaction network (RIN) of the energy minimum structure was obtained from the free energy landscape using Cytoscape v3.9.1 (54).

3.4.4. MM-PBSA Calculation

"Free energy" refers to a measure of internal energy of the system that can be utilized for its work. It is the major driving force of all bimolecular processes like protein folding and unfolding, biochemical reactions and protein−ligand binding interactions (55, 56). Thus, accurate predictions of the free energy are of utmost importance during the course of

ligand−protein binding interaction studies. The molecular mechanics energies in combination with the Poisson−Boltzmann and the surface area in continuation to solvation (MM-PBSA) is a popular method for binding free energy estimation with great success and reproducibility (24). The enthalpy and entropy contributions were calculated for the energy minimum structure obtained from the free energy landscape diagram along with its two adjacent frames of the trajectory. The GROMACS output trajectory was fitted and PBC conditions were removed before running the calculations with gmx_MMPBSA; (57) here we have used a single trajectory approach to calculate the binding free energy differences. gmx_MMPBSA is a tool written in Python 3.8 (58) that combines the functionality from GROMACS and AmberTools (59) in order to build input files in an accurate manner that can be reproducible so as to perform the end-state free energy calculations. The work was carried out in three crucial steps; (i) preparation where the MMPBSA.py calculation engine provided in the gmx_MMPBSA was used to carry out the calculations and where the MD simulation output topology files from GROMACS were used for conversion into Amber topology format; (ii) multiple calculations carried out for binding free energies with different solvation models (PB, GB, or 3DRISM), and; (iii) visualization and analysis performed once the calculations were complete by the help of a graphical user interface application (gmx_MMPBSA_ana). MM-PBSA is a well-established methodology for the estimation of binding free energy and correlates well with in vitro data (60, 61).

3.4.5. In-Silico BBB Predictions

The in-silico blood−brain permeability predictions for the PPIs under study were carried out using the “CBligand-BBB predictor” Web server (https://www.cbligand.org/ BBB/) (29). CBligand-BBB predictor is built on support vector machine (SVM) and LiCABEDS (62) algorithms along with four different types of fingerprints, of which we used MACCS (63)

fingerprint for our prediction. The predictor gives positive values if the given compound can readily cross the BBB and vice versa.

3.5. Conclusion

Although it is undeniable that proton pump inhibitors (PPIs) are currently invaluable and effective drugs for the management and treatment of a variety of gastric related disorders, there are accumulating reports of adverse drug reactions in relation to excessive and/or prolonged use in patients, particularly elderly patients (64-66). An early diagnosis is an important aspect for proper management of AD and other dementias, e.g., to eliminate or reduce the impact of the known risk factors of AD and/or to initiate therapeutic interventions as soon as possible before occurrence of severe neuronal degeneration. A prominent target is ChAT, which is the main cholinergic enzyme responsible for the biosynthesis of acetylcholine.

As a continuous program to find novel ChAT ligands, we have previously reported that several PPIs act as ChAT inhibitors with high potential to be developed into diagnostic probes for the early diagnosis of cholinergic decline (17, 67). In this Chapter, we continued our study on PPIs by employing a comprehensive computational technique of combining molecular docking and classical molecular dynamics (MD) simulations along with MM-PBSA to calculate the binding free energy, to gain insight into the molecular mechanism of interaction and binding of PPIs to ChAT. The results suggested that PPIs display strong binding interaction with ChAT and that they possess good binding affinity toward ChAT as compared with α-NETA, one of the known inhibitors of ChAT.

Molecular dynamic analysis of 200 ns trajectories indicated that PPIs formed stable complexes with ChAT within this simulation time frame. Subsequent related analyses of the stability of the system indicated that the interaction with the HIS324 residue of ChAT was important for the stability of the formed ChAT−PPI complex since it showed polar interaction with the pyridine ring of the PPIs, as deduced by the global energy minima analysis. In addition, the

VAL555 and ILE330 amino residues of ChAT play a major role in the geometric orientation of the R and S enantiomers of the PPIs in the binding tunnel of ChAT and thus aid in the stabilization of the PPI in the binding tunnel. Altogether, given that the HIS324 residue lies in the center of the catalytic tunnel of ChAT and that it is primarily responsible for the transfer of the acetyl group from acetyl-CoA to the choline and thereby the synthesis of acetylcholine, (38, 68) our findings indicate that the mechanism of action of PPIs as inhibitors of ChAT is governed by their interference with the HIS324 residue. Overall, we conclude that the chemical scaffold of PPIs could be used to simplify structures in strategic development of more potent ChAT ligands with optimal pharmacokinetic and pharmacodynamics properties along with good oral bioavailability and BBB permeability.

3.6. References

1. Kim J-H, Oh J-K, Kim Y-H, Kwon M-J, Kim J-H, Choi H-G. Association between proton pump inhibitor use and Parkinson's disease in a Korean population. Pharmaceuticals. 2022;15(3):327.
2. Strand DS, Kim D, Peura DA. 25 years of proton pump inhibitors: a comprehensive review. Gut and liver. 2017;11(1):27.
3. Shin JM, Sachs G. Pharmacology of proton pump inhibitors. Current gastroenterology reports. 2008;10(6):528-34.
4. Shamburek RD, Schubert ML. Pharmacology of gastric acid inhibition. Baillière's clinical gastroenterology. 1993;7(1):23-54.
5. Zhang P, Li Z, Chen P, Zhang A, Zeng Y, Zhang X, et al. Regular proton pump inhibitor use and incident dementia: population-based cohort study. BMC medicine. 2022;20(1):271.
6. Ahn N, Nolde M, Günter A, Güntner F, Gerlach R, Tauscher M, et al. Emulating a target trial of proton pump inhibitors and dementia risk using claims data. European Journal of Neurology. 2022;29(5):1335-43.
7. Weller J, Budson A. Current understanding of Alzheimer's disease diagnosis and treatment. F1000Research. 2018;7.
8. Gomm W, von Holt K, Thomé F, Broich K, Maier W, Fink A, et al. Association of proton pump inhibitors with risk of dementia: a pharmacoepidemiological claims data analysis. JAMA neurology. 2016;73(4):410-6.
9. Haenisch B, von Holt K, Wiese B, Prokein J, Lange C, Ernst A, et al. Risk of dementia in elderly patients with the use of proton pump inhibitors. European archives of psychiatry and clinical neuroscience. 2015;265:419-28.
10. Tai S-Y, Chien C-Y, Wu D-C, Lin K-D, Ho B-L, Chang Y-H, et al. Risk of dementia from proton pump inhibitor use in Asian population: a nationwide cohort study in Taiwan. PloS one. 2017;12(2):e0171006.
11. Lam JR, Schneider JL, Zhao W, Corley DA. Proton pump inhibitor and histamine 2 receptor antagonist use and vitamin B12 deficiency. Jama. 2013;310(22):2435-42.

12. Kumar R, Kumar A, Nordberg A, Långström B, Darreh-Shori T. Proton pump inhibitors act with unprecedented potencies as inhibitors of the acetylcholine biosynthesizing enzyme—a plausible missing link for their association with incidence of dementia. Alzheimer's & Dementia. 2020;16(7):1031-42.
13. Oda Y. Choline acetyltransferase: the structure, distribution and pathologic changes in the central nervous system. Pathology international. 1999;49(11):921-37.
14. H Ferreira-Vieira T, M Guimaraes I, R Silva F, M Ribeiro F. Alzheimer's disease: targeting the cholinergic system. Current neuropharmacology. 2016;14(1):101-15.
15. Baker BR, Gibson RE. Irreversible enzyme inhibitors. 181. Inhibition of brain choline acetyltransferase by derivatives of 4-stilbazole. Journal of Medicinal Chemistry. 1971;14(4):315-22.
16. Sastry B, Jaiswal N, Owens L, Janson V, Moore R. 2-(alpha-Naphthoyl) ethyltrimethylammonium iodide and its beta-isomer: new selective, stable and fluorescent inhibitors of choline acetyltransferase. Journal of Pharmacology and Experimental Therapeutics. 1988;245(1):72-80.
17. Kumar R, Långström B, Darreh-Shori T. Novel ligands of Choline Acetyltransferase designed by in silico molecular docking, hologram QSAR and lead optimization. Scientific reports. 2016;6(1):31247.
18. Bolhuis P. Sampling kinetic protein folding pathways using all-atom models. Computer Simulations in Condensed Matter Systems: From Materials to Chemical Biology Volume 1: Springer; 2006. p. 393-433.
19. Sneha P, Doss CGP. Molecular dynamics: new frontier in personalized medicine. Advances in protein chemistry and structural biology. 2016;102:181-224.
20. Pace CN, Shirley BA, McNutt M, Gajiwala K. Forces contributing to the conformational stability of proteins. The FASEB journal. 1996;10(1):75-83.
21. Zhang D, Lazim R. Application of conventional molecular dynamics simulation in evaluating the stability of apomyoglobin in urea solution. Scientific Reports. 2017;7(1):44651.
22. Kitao A. Principal component analysis and related methods for investigating the dynamics of biological macromolecules. J. 2022;5(2):298-317.
23. Prada-Gracia D, Gómez-Gardeñes J, Echenique P, Falo F. Exploring the free energy landscape: from dynamics to networks and back. PLoS computational biology. 2009;5(6):e1000415.
24. Genheden S, Ryde U. The MM/PBSA and MM/GBSA methods to estimate ligand-binding affinities. Expert opinion on drug discovery. 2015;10(5):449-61.
25. Salmaso V, Moro S. Bridging molecular docking to molecular dynamics in exploring ligand-protein recognition process: An overview. Frontiers in pharmacology. 2018;9:923.
26. Naqvi AA, Mohammad T, Hasan GM, Hassan MI. Advancements in docking and molecular dynamics simulations towards ligand-receptor interactions and structure-function relationships. Current topics in medicinal chemistry. 2018;18(20):1755-68.
27. Rocchia W, Masetti M, Cavalli A. Enhanced sampling methods in drug design. Physico-Chemical and Computational Approaches to Drug Discovery The Royal Society of Chemistry. 2012:273-301.
28. Valsson O, Tiwary P, Parrinello M. Enhancing important fluctuations: Rare events and metadynamics from a conceptual viewpoint. Annual review of physical chemistry. 2016;67(1):159-84.
29. Liu H, Wang L, Lv M, Pei R, Li P, Pei Z, et al. AlzPlatform: an Alzheimer's disease domain-specific chemogenomics knowledgebase for polypharmacology and target identification research. Journal of chemical information and modeling. 2014;54(4):1050-60.

30. Liang J-F, Chen Y-T, Fuh J-L, Li S-Y, Chen T-J, Tang C-H, et al. Proton pump inhibitor-related headaches: a nationwide population-based case-crossover study in Taiwan. Cephalalgia. 2015;35(3):203-10.
31. Ortiz-Guerrero G, Amador-Muñoz D, Calderón-Ospina CA, López-Fuentes D, Nava Mesa MO. Proton pump inhibitors and dementia: physiopathological mechanisms and clinical consequences. Neural plasticity. 2018;2018(1):5257285.
32. Rosenberg G. Blood-brain barrier permeability in aging and Alzheimer's disease. The journal of prevention of Alzheimer's disease. 2014;1(3):138.
33. Hussain B, Fang C, Chang J. Blood–brain barrier breakdown: an emerging biomarker of cognitive impairment in normal aging and dementia. Frontiers in neuroscience. 2021;15:688090.
34. Friesner RA, Murphy RB, Repasky MP, Frye LL, Greenwood JR, Halgren TA, et al. Extra precision glide: Docking and scoring incorporating a model of hydrophobic enclosure for protein− ligand complexes. Journal of medicinal chemistry. 2006;49(21):6177-96.
35. Kim S, Thiessen PA, Bolton EE, Chen J, Fu G, Gindulyte A, et al. PubChem substance and compound databases. Nucleic acids research. 2016;44(D1):D1202-D13.
36. Shivakumar D, Harder E, Damm W, Friesner RA, Sherman W. Improving the prediction of absolute solvation free energies using the next generation OPLS force field. Journal of chemical theory and computation. 2012;8(8):2553-8.
37. Zhou Q, Yan X-F, Pan W-S, Zeng S. Is the required therapeutic effect always achieved by racemic switch of proton-pump inhibitors? World journal of gastroenterology: WJG. 2008;14(16):2617.
38. Kim A-R, Rylett RJ, Shilton BH. Substrate binding and catalytic mechanism of human choline acetyltransferase. Biochemistry. 2006;45(49):14621-31.
39. Schrödinger R. Protein preparation wizard, maestro, macromodel, QPLD-dock, and Pymol. Schrödinger, LLC. 2016;97204.
40. Schrödinger L. Maestro, Version 10.5. New York, NY, USA. 2016;1.
41. Repasky MP, Shelley M, Friesner RA. Flexible ligand docking with Glide. Current protocols in bioinformatics. 2007;18(1):8.12. 1-8.. 36.
42. Abraham MJ, Murtola T, Schulz R, Páll S, Smith JC, Hess B, et al. GROMACS: High performance molecular simulations through multi-level parallelism from laptops to supercomputers. SoftwareX. 2015;1:19-25.
43. Huang J, Rauscher S, Nawrocki G, Ran T, Feig M, De Groot BL, et al. CHARMM36m: an improved force field for folded and intrinsically disordered proteins. Nature methods. 2017;14(1):71-3.
44. Baidya AT, Kumar A, Kumar R, Darreh-Shori T. Allosteric binding sites of Aβ peptides on the acetylcholine synthesizing enzyme ChAT as deduced by in silico molecular modeling. International Journal of Molecular Sciences. 2022;23(11):6073.
45. Jo S, Kim T, Iyer VG, Im W. CHARMM-GUI: a web-based graphical user interface for CHARMM. Journal of computational chemistry. 2008;29(11):1859-65.
46. Jo S, Cheng X, Lee J, Kim S, Park SJ, Patel DS, et al. CHARMM-GUI 10 years for biomolecular modeling and simulation. Journal of computational chemistry. 2017;38(15):1114-24.
47. Morozova TI, García NA, Barrat J-L. Temperature dependence of thermodynamic, dynamical, and dielectric properties of water models. The Journal of Chemical Physics. 2022;156(12).
48. Jo S, Kim T, Im W. Automated builder and database of protein/membrane complexes for molecular dynamics simulations. PloS one. 2007;2(9):e880.
49. Hess B, Bekker H, Berendsen HJ, Fraaije JG. LINCS: a linear constraint solver for molecular simulations. Journal of computational chemistry. 1997;18(12):1463-72.

50. Panwar A, Kumar A. In-silico analysis and molecular dynamics simulations of lysozyme by GROMACS 2020.2. Annals of the Romanian Society for Cell Biology. 2021;25(6):9679-85.
51. Basconi JE, Shirts MR. Effects of temperature control algorithms on transport properties and kinetics in molecular dynamics simulations. Journal of chemical theory and computation. 2013;9(7):2887-99.
52. Martoňák R, Laio A, Parrinello M. Predicting crystal structures: the Parrinello-Rahman method revisited. Physical review letters. 2003;90(7):075503.
53. David CC, Jacobs DJ. Principal component analysis: a method for determining the essential dynamics of proteins. Protein dynamics: Methods and protocols. 2014:193-226.
54. Saito R, Smoot ME, Ono K, Ruscheinski J, Wang P-L, Lotia S, et al. A travel guide to Cytoscape plugins. Nature methods. 2012;9(11):1069-76.
55. Xue W, Yang F, Wang P, Zheng G, Chen Y, Yao X, et al. What contributes to serotonin–norepinephrine reuptake inhibitors' dual-targeting mechanism? The key role of transmembrane domain 6 in human serotonin and norepinephrine transporters revealed by molecular dynamics simulation. ACS chemical neuroscience. 2018;9(5):1128-40.
56. Xue W, Fu T, Deng S, Yang F, Yang J, Zhu F. Molecular mechanism for the allosteric inhibition of the human serotonin transporter by antidepressant escitalopram. ACS chemical neuroscience. 2022;13(3):340-51.
57. Valdés-Tresanco MS, Valdés-Tresanco ME, Valiente PA, Moreno E. gmx_MMPBSA: a new tool to perform end-state free energy calculations with GROMACS. Journal of chemical theory and computation. 2021;17(10):6281-91.
58. Hettinger R. What's new in Python 3.8. Python Docs. 2019.
59. Case D, Betz R, Botello-Smith W, Cerutti D, Cheatham III T, Darden T, et al. AmberTools 16. University of California, San Francisco. 2016.
60. Card GL, Blasdel L, England BP, Zhang C, Suzuki Y, Gillette S, et al. A family of phosphodiesterase inhibitors discovered by cocrystallography and scaffold-based drug design. Nature biotechnology. 2005;23(2):201-7.
61. Fu T, Jin Z, Xiu Z, Li G. Binding free energy estimation for protein-ligand complex based on MM-PBSA with various partial charge models. Current pharmaceutical design. 2013;19(12):2293-307.
62. Ma C, Wang L, Xie X-Q. Ligand classifier of adaptively boosting ensemble decision stumps (LiCABEDS) and its application on modeling ligand functionality for 5HT-subtype GPCR families. Journal of chemical information and modeling. 2011;51(3):521-31.
63. Cereto-Massagué A, Ojeda MJ, Valls C, Mulero M, Garcia-Vallvé S, Pujadas G. Molecular fingerprint similarity search in virtual screening. Methods. 2015;71:58-63.
64. Choi HG, Kim J-H, Kim JH, Kim ES, Park HY, Min K-W, et al. Associations between proton pump inhibitors and Alzheimer's disease: a nested case–control study using a Korean nationwide health screening cohort. Alzheimer's Research & Therapy. 2022;14(1):91.
65. Bando T, di Pace L, Lapa M, Chehter E. Proton pump inhibitors: Are they safe? Gastroenterol Hepatol Open Access. 2022;13:34.
66. Gray SL, Walker RL, Dublin S, Yu O, Aiello Bowles EJ, Anderson ML, et al. Proton pump inhibitor use and dementia risk: Prospective population-based study. Journal of the American Geriatrics Society. 2018;66(2):247-53.
67. Kumar R, Kumar A, Långström B, Darreh-Shori T. Discovery of novel choline acetyltransferase inhibitors using structure-based virtual screening. Scientific reports. 2017;7(1):16287.
68. Green KD, Porter VR, Zhang Y, Garneau-Tsodikova S. Redesign of cosubstrate specificity and identification of important residues for substrate binding to hChAT. Biochemistry. 2010;49(29):6219-27.